8-3-2021

High Sensitivity Multi-Axes Rotation Sensing Using Large Momentum Transfer Point Source Atom Interferometry

Jinyang Li
Northwestern University, li27j@u.northwestern.edu

Gregório R. M. da Silva
Northwestern University, gregoriorabelo2022@u.northwestern.edu

Wayne Cheng-Wei Huang
Northwestern University, wayne.huang@uni-goettingen.de

Mohamed Fouda
Northwestern University, mfatouh@gmail.com

Jason Bonacum
Digital Optics Technologies, jason@digital-optics-inc.com

See next page for additional authors

atoms

MDPI

Article

High Sensitivity Multi-Axes Rotation Sensing Using Large Momentum Transfer Point Source Atom Interferometry

Jinyang Li [1,*], Gregório R. M. da Silva [1], Wayne C. Huang [1], Mohamed Fouda [2], Jason Bonacum [2], Timothy Kovachy [1] and Selim M. Shahriar [1,3]

[1] Department of Physics and Astronomy, Northwestern University, Evanston, IL 60208, USA; gregoriorabelo2022@u.northwestern.edu (G.R.M.d.S.); wayne.huang@uni-goettingen.de (W.C.H.); timothy.kovachy@northwestern.edu (T.K.); shahriar@northwestern.edu (S.M.S.)
[2] Digital Optics Technologies, Rolling Meadows, IL 60008, USA; mfatouh@gmail.com (M.F.); jason@digital-optics-inc.com (J.B.)
[3] Department of ECE, Northwestern University, Evanston, IL 60208, USA
* Correspondence: li27j@u.northwestern.edu

Abstract: A point source interferometer (PSI) is a device where atoms are split and recombined by applying a temporal sequence of Raman pulses during the expansion of a cloud of cold atoms behaving approximately as a point source. The PSI can work as a sensitive multi-axes gyroscope that can automatically filter out the signal from accelerations. The phase shift arising from the rotations is proportional to the momentum transferred to each atom from the Raman pulses. Therefore, by increasing the momentum transfer, it should be possible to enhance the sensitivity of the PSI. Here, we investigate the degree of enhancement in sensitivity that could be achieved by augmenting the PSI with large momentum transfer (LMT) employing a sequence of many Raman pulses with alternating directions. We analyze how factors such as Doppler detuning, spontaneous emission, and the finite initial size of the atomic cloud compromise the advantage of LMT and how to find the optimal momentum transfer under these limitations, with both the semi-classical model and a model under which the motion of the center of mass of each atom is described quantum mechanically. We identify a set of realistic parameters for which LMT can improve the PSI by a factor of nearly 40.

Keywords: quantum gyroscope; atom interferometry; point source atom interferometer

Citation: Li, J.; R. M. da Silva, G.; Huang, W.C.; Fouda, M.; Bonacum, J.; Kovachy, T.; Shahriar, S.M. High Sensitivity Multi-Axes Rotation Sensing Using Large Momentum Transfer Point Source Atom Interferometry. *Atoms* **2021**, *9*, 51. https://doi.org/10.3390/atoms9030051

Academic Editor: Andrea Bertoldi

Received: 18 May 2021
Accepted: 28 July 2021
Published: 3 August 2021

1. Introduction

Atom interferometry offers the potential to deliver high-performance, compact, and robust gyroscopes that are suitable for inertial navigation applications. Critical requirements for such an atomic gyroscope include a high sensitivity to rotations and the ability to distinguish between signals arising from rotations and accelerations. Here, we describe a multi-axes gyroscope based on the combination of point source interferometry (PSI) [1–3] and large momentum transfer (LMT) beam splitters [4,5] which are well-suited to meet these requirements. In a PSI, Raman pulses are applied during the expansion of a point source of atoms. The pulses are a pair of counter-propagating laser beams that drive two-photon Raman transitions [6], serving as the beam splitters and mirrors for a Mach–Zehnder light-pulse atom interferometer [7–13], as shown in Figure 1. The interferometer phase response to rotation scales linearly with the velocity difference of the atoms in the two arms, while the response to acceleration is independent of the atomic velocity. Because of this difference, the signal in a PSI allows rotation and acceleration to be distinguished. The PSI can also determine both components of the rotation vector that are orthogonal to the laser pulses, thus realizing a multi-axes gyroscope. It should be noted that there are other techniques that can also distinguish between rotation and acceleration [9–13]. However, a key practical advantage of the PSI is that it only requires a single atom cloud and Raman beams along a single axis, in contrast to other methods.

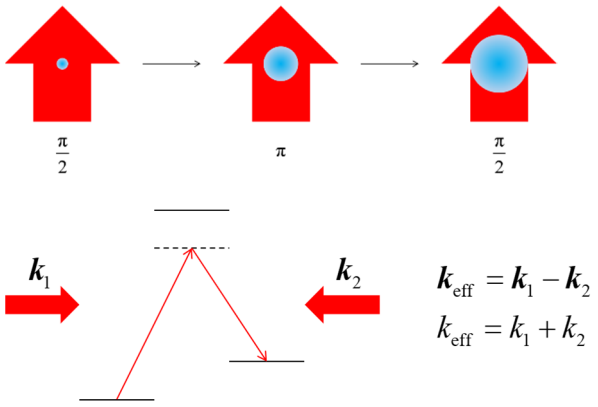

Figure 1. Schematic illustration of the basic process underlying the conventional PSI. The blue circle is the atom cloud and the red arrows are the Raman pulses. A temporal sequence of Raman pulses is applied during the expansion of the atom cloud (**top**), and each Raman pulse is a pair of counter-propagating light beams that drive a two-photon transition (**bottom**).

The LMT beam splitters we consider involve the use of tailored laser pulse sequences to increase the momentum splitting, and therefore the velocity difference, between the two arms of the interferometer. Via the Sagnac effect, the rotation sensitivity of a gyroscope is proportional to the area enclosed by an interferometer. The enclosed area is proportional to the velocity difference induced by the beam splitter; as such, the rotation sensitivity scales linearly with the momentum transferred by the laser pulses during the beam splitting process.

The conventional model of the light-pulse interferometer as well as the PSI makes the approximation that each atom has a well-defined velocity as well as a well-defined position. This model is apparently inadequate for describing the behavior of a PSI accurately for several reasons. The first is that the wave packets of cold atoms cover large spatial extents and thus do not have trajectories that enclose a well-defined area. The second is that atoms are in superpositions of many momentum eigenstates, with each of them seeing a different light frequency. Yet the model has proven to be quite useful in predicting the behavior of a light-pulse interferometer as well as the PSI in most circumstances of experimental relevance. As such, in the initial stage of our analysis, some of the salient features of the effect of large momentum transfer on the PSI are extracted from the conventional model. Later on, we augment the analysis with a more rigorous model wherein the center of mass motion of each atom is treated quantum mechanically, represented as a superposition of plane waves, since it is not a priori obvious, without experimental results, whether the semiclassical model would be adequate when the PSI is augmented by large momentum transfer.

The rest of the paper is organized as follows. In Section 2, we use the conventional model to summarize first the basic properties of a PSI without large momentum transfer (LMT). We then use the same model to determine how the signal for a PSI would be modified in the presence of LMT, without taking into account non-idealities such as Doppler detuning and spontaneous emission. We also describe how the signal for an LMT–PSI is modified when the point source is replaced by a source with a finite extent and determine how the enhancement in sensitivity varies as function of the degree of momentum transfer under the LMT process, as well as the initial size of the source. In Section 3, we present the augmented quantum model where the center mass motion of the atom is treated quantum mechanically. We consider first the ideal case where an atom is in a pure state. This is followed by a consideration of a situation where the atoms are thermalized in a harmonic oscillator potential before being released for the LMT–PSI process, taking into account quantum statistics. We conclude this section with a discussion of how the results of this augmented quantum model compare with those of the conventional semi-classical model under various conditions. Specifically, we find that for thermal atoms, the predictions of

these two models do not differ significantly. In Section 4, we analyze the combined effect of all non-idealities, including Doppler detuning, spontaneous emission, and the finite size of the source, using the augmented quantum model. However, in order to be able to carry out an analytical estimation of the enhancement in sensitivity expected for a significant degree of LMT, we make some simplifying assumptions that render the model essentially equivalent to that of the conventional semi-classical model. We expect that a full-blown version of the augmented quantum model would produce results that agree closely with the conclusions reached in this section. But such a full-blown analysis requires enormous computational resources; given that the difference between the results produced by the semi-classical analysis and the augmented quantum model is very small, undertaking such an analysis was not deemed critically important at this point. Instead, it is expected, subject to experimental verification, that the predictions of the effectively semi-classical model would be adequate. Finally, we summarize the results in Section 5.

2. Conventional Model

As noted above, the conventional model of a PSI makes the approximation that each atom has a well-defined velocity as well as a well-defined position. Therefore, the atoms follow definitive trajectories that enclose an area. Specifically, the enclosed area is $\boldsymbol{A} = (\boldsymbol{r}/2) \times (\hbar \boldsymbol{k}_t T/m)$, where $\hbar \boldsymbol{k}_t$ is the differential momentum transferred to an atom from the initial light pulse, $\boldsymbol{r}$ is the displacement of the atoms, T is half of the total time elapsed, from splitting to recombination, and m is the mass of each atom [14]. The Sagnac phase shift is proportional to the enclosed area according to the expression $\phi = 2\omega_C \boldsymbol{\Omega} \cdot \boldsymbol{A}/c^2$, where $\omega_C = mc^2/\hbar$ is the Compton frequency of each atom [15], and $\boldsymbol{\Omega}$ is the angular velocity of the rotation. It then follows that the phase shift can be expressed as $\phi = (\boldsymbol{k}_t \times \boldsymbol{\Omega} T) \cdot \boldsymbol{r} \equiv \boldsymbol{k}_\Omega \cdot \boldsymbol{r}$. The measured signal is the spatial distribution of the ground state population, given by the expectation value of the projection operator $P_g(\boldsymbol{r}) \equiv |g, \boldsymbol{r}\rangle\langle g, \boldsymbol{r}|$. As such, the signal can be expressed [8] as $\langle P_g(\boldsymbol{r})\rangle = f(\boldsymbol{r})(1 + \cos \boldsymbol{k}_\Omega \cdot \boldsymbol{r})/2$, which is a pattern of spatial fringes dictated by the wave number $\boldsymbol{k}_\Omega$, multiplied by $f(\boldsymbol{r})$, the final profile of the atomic cloud. With this model, it seems obvious that by increasing $\boldsymbol{k}_t$, we can increase $\boldsymbol{k}_\Omega$, thus reducing the fringe spacing, and thereby increasing the sensitivity of the PSI.

To determine quantitatively the density of fringes, we have to compute the Fourier transform of the pattern. Experimentally, this Fourier transform can be observed in real time using a lens in the system for imaging the atom cloud. Thus, our signal is expressed as $\widetilde{P}_g\left(\tilde{\boldsymbol{k}}\right) = \int d\boldsymbol{r}\, e^{-i\tilde{\boldsymbol{k}}\cdot\boldsymbol{r}} \langle P_g(\boldsymbol{r})\rangle$, where $P_g(\boldsymbol{r})$ is the position space projection operator for atoms in the ground state, as defined earlier. It should be noted that $\widetilde{P}_g\left(\tilde{\boldsymbol{k}}\right)$ is different from $P_g(\boldsymbol{k}) \equiv |g, \boldsymbol{k}\rangle\langle g, \boldsymbol{k}|$, the momentum space projection operator for atoms in the ground state. The semi-classical model gives a signal that can be expressed as:

$$\widetilde{P}_g\left(\tilde{\boldsymbol{k}}\right) = \mathcal{F}\left[\frac{1}{2} f(\boldsymbol{r})(1 + \cos \boldsymbol{k}_\Omega \cdot \boldsymbol{r})\right] = \frac{1}{2}\widetilde{f}\left(\tilde{\boldsymbol{k}}\right) + \frac{1}{4}\widetilde{f}\left(\tilde{\boldsymbol{k}} - \boldsymbol{k}_\Omega\right) + \frac{1}{4}\widetilde{f}\left(\tilde{\boldsymbol{k}} + \boldsymbol{k}_\Omega\right) \quad (1)$$

where $\widetilde{f}\left(\tilde{\boldsymbol{k}}\right) \equiv \mathcal{F}[f(\boldsymbol{r})]$ is the Fourier transform of the profile of the atomic cloud. The spatial fringes representing $\langle P_g(\boldsymbol{r})\rangle$ and the corresponding Fourier transforms given by $\widetilde{P}_g\left(\tilde{\boldsymbol{k}}\right)$ derived from the semi-classical model are depicted in Figure 2. Panel A shows plots for $k_t = k_{\text{eff}}$ and panel B shows plots for $k_t = 3k_{\text{eff}}$. In each panel, (a) is the plot of $\langle P_g(\boldsymbol{r})\rangle = f(\boldsymbol{r})(1 + \cos \boldsymbol{k}_\Omega \cdot \boldsymbol{r})/2$, with $f(\boldsymbol{r}) = \exp\left(-\boldsymbol{r}^2/2\sigma_f^2\right)$, in the plane perpendicular to $\boldsymbol{k}_t$, (b) is the cross section at the dashed line in (a), (c) is the plot of $\widetilde{P}_g\left(\tilde{\boldsymbol{k}}\right)$ in the plane perpendicular to $\boldsymbol{k}_t$, and (d) is the cross section at the dashed line of (c). In the

Fourier domain, the distance from a signal peak, for example, $\widetilde{f}\left(\tilde{\boldsymbol{k}}-\boldsymbol{k}_{\Omega}\right)/4$, to the central peak $\widetilde{f}\left(\tilde{\boldsymbol{k}}\right)/2$, is $\boldsymbol{k}_{\Omega}$, which is proportional to the angular velocity we want to measure. The height of the signal peak h corresponds to the contrast of the fringes, and ideally $h^{\text{ideal}}=1/4$.

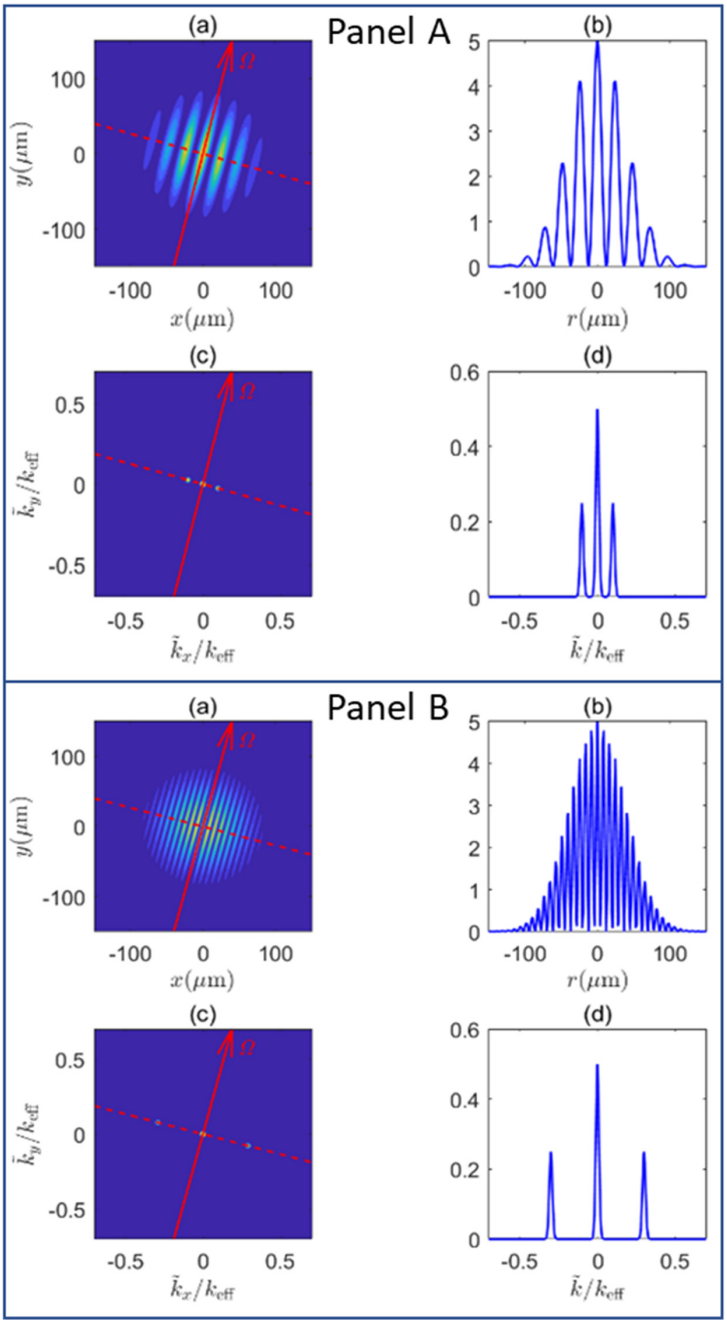

Figure 2. Signals for the conventional PSI and the PSI–LMT without considering the detuning effect. **Panel A** corresponds to $k_{\text{t}}=k_{\text{eff}}$ and **Panel B** corresponds to $k_{\text{t}}=3k_{\text{eff}}$. In each panel, (**a**) is the plot of $\langle P_g(\boldsymbol{r})\rangle = f(\boldsymbol{r})(1+\cos\boldsymbol{k}_{\Omega}\cdot\boldsymbol{r})/2$, with $f(\boldsymbol{r})=\exp\left(-\boldsymbol{r}^2/2\sigma_{\text{f}}^2\right)$, in the plane perpendicular to $\boldsymbol{k}_{\text{t}}$, (**b**) is the cross section at the dashed line in (**a**), (**c**) is the plot of $\widetilde{P}_g\left(\tilde{\boldsymbol{k}}\right)$ in the plane perpendicular to $\boldsymbol{k}_{\text{t}}$, and (**d**) is the cross section at the dashed line of (**c**). The orientation of the signal indicates the direction of the angular velocity.

In this model, for an ideal point source, the final position of an atom is determined by its initial velocity. The velocity spread of the atoms is given by the Boltzmann distribution characterized by the temperature of the atomic cloud. Therefore, the final population distribution of the atoms has a three-dimensional Gaussian profile, $\exp\left(-\boldsymbol{r}^2/2\sigma_\mathrm{f}^2\right)$, where σ_f describes the final size of the atomic cloud, determined by the initial velocity spread and the expansion time. Thus, the final spatial distribution of the ground state atoms can be expressed as $n_\mathrm{ps}(\boldsymbol{r}) \equiv \langle P_g(\boldsymbol{r})\rangle = \exp\left(-\boldsymbol{r}^2/2\sigma_\mathrm{f}^2\right)(1+\cos \boldsymbol{k}_\Omega \cdot \boldsymbol{r})/2$. In the plots shown in Figure 2, we assumed such a Gaussian envelope for the ground state populations, with an arbitrarily chosen value of σ_f. Here, Figure 2a in each panel is simply a plot of this expression for $n_\mathrm{ps}(\boldsymbol{r})$.

This model can also be used to analyze the effect of the finite size of the initial atomic cloud. For this analysis, we assumed that the Raman pulses were along the z-direction, while the angular velocity vector was in the y-direction. Then the interference fringes were oriented in the x-direction. For simplicity, we looked at a slice of the atomic cloud in the x-direction, for $y = z = 0$. The population in this slice can be expressed as $n_\mathrm{ps}(x) = \exp\left(-x^2/2\sigma_\mathrm{f}^2\right)(1+\cos k_\Omega x)/2$. The initial cloud of a finite size is a collection of the many ideal point sources. We assumed the initial distribution of the atomic cloud to be of the form $n_0(x) = \exp\left(-x^2/2\sigma_0^2\right)$. The final spatial distribution of the ground state atoms is then the convolution of n_0 and n_ps:

$$n_\mathrm{f} = \int n_0(x_0) n_\mathrm{ps}(x - x_0)\mathrm{d}x = n_0 * n_\mathrm{ps} \tag{2}$$

It is easy to see that n_f has the form of $(1 + 4h\cos k'_\Omega x)/2$ where [2]

$$k'_\Omega = k_\Omega\left[1 - (\sigma_0/\sigma_\mathrm{f})^2\right] \tag{3}$$

$$h = h^\mathrm{ideal}\exp\left(-\frac{1}{2}k_\Omega^2\sigma_0^2\left[1 - \left(\frac{\sigma_0}{\sigma_\mathrm{f}}\right)^2\right]\right) \tag{4}$$

Equation (3) implies that the signal peak is at a distance k'_Ω away from the central peak in the Fourier transform domain. Thus, if the point source has a finite size, the signal peak moves closer to the central peak and the height of the signal peak is reduced. The uncertainty in the position of the signal peak $\delta k'_\Omega$ in turn determines the uncertainty in the determination of Ω. Specifically, from the expression of $\boldsymbol{k}_\Omega$ stated earlier, and assuming that $\boldsymbol{k}_\mathrm{t}$ is orthogonal to $\boldsymbol{\Omega}$, it follows from Equation (3) that $\delta\Omega = \delta k'_\Omega / k_\mathrm{t} T\left[1 - (\sigma_0/\sigma_\mathrm{f})^2\right]$. In general, the uncertainty of a signal is the linewidth divided by the signal-to-noise ratio. Using this rule, we can write that $\delta k'_\Omega = \beta\gamma/\sqrt{h}$, where γ is the width of the signal peak and β is a constant coefficient. It then follows that $(\delta\Omega)^{-1} = k_\mathrm{t} T\sqrt{h}\left[1 - (\sigma_0/\sigma_\mathrm{f})^2\right]/\beta\gamma$. Since the signal is in the Fourier transform domain, γ is approximately the inverse of the final size of the atomic cloud. Therefore, γ is determined primarily by the free expansion and is not affected significantly by the LMT process. Thus, we see that the larger the final atomic cloud size is, the smaller γ is, and the smaller $\delta\Omega$ is. This reduction in $\delta\Omega$ can be understood physically by noting first that the width (i.e., γ) of each of the peaks in the Fourier Transform domain becomes smaller for larger final atomic clouds. Since the uncertainty in the measured value of the rotation rate is proportional to this width, it then follows that a larger final atomic cloud yields a smaller value of $\delta\Omega$.

To compare LMT–PSI's with different values of $k_\mathrm{t} = Nk_\mathrm{eff}$, we assumed that the atomic clouds ended up with the same final size, and therefore the same γ, independent of the value of N. We defined an improvement parameter $\varepsilon \equiv \delta\Omega_{Nk_\mathrm{eff}}/\delta\Omega_{k_\mathrm{eff}} = N\left[1 - (\sigma_0/\sigma_\mathrm{f})^2\right]\sqrt{h_{Nk_\mathrm{eff}}/h_{k_\mathrm{eff}}}$. In experiments, the final size of the atomic cloud is determined by the size of the apparatus, and thus can be considered a rigid constraint. For concreteness, we assumed the value of σ_f to be 1 cm. We also assumed the initial temperature to be 6 μK, a value that can be achieved typically with optical molasses [2]. The

expansion time is related to the initial and final sizes of the atomic cloud according to the expression $\sigma_f^2 = \sigma_0^2 + (k_B T_K/m)(2T)^2$. In Figure 3, we show a plot of the improvement factor versus the momentum transfer, with two different initial sizes of the atomic cloud and two angular velocities. The red curves are the plots for $\sigma_0 = 0.1$ mm while the blue curves are for $\sigma_0 = 0.2$ mm. The solid (dashed) curves correspond to an angular velocity of 1 (2) μHz. We can see that LMT can improve the PSI more for smaller initial atomic clouds and for measuring a smaller angular velocity.

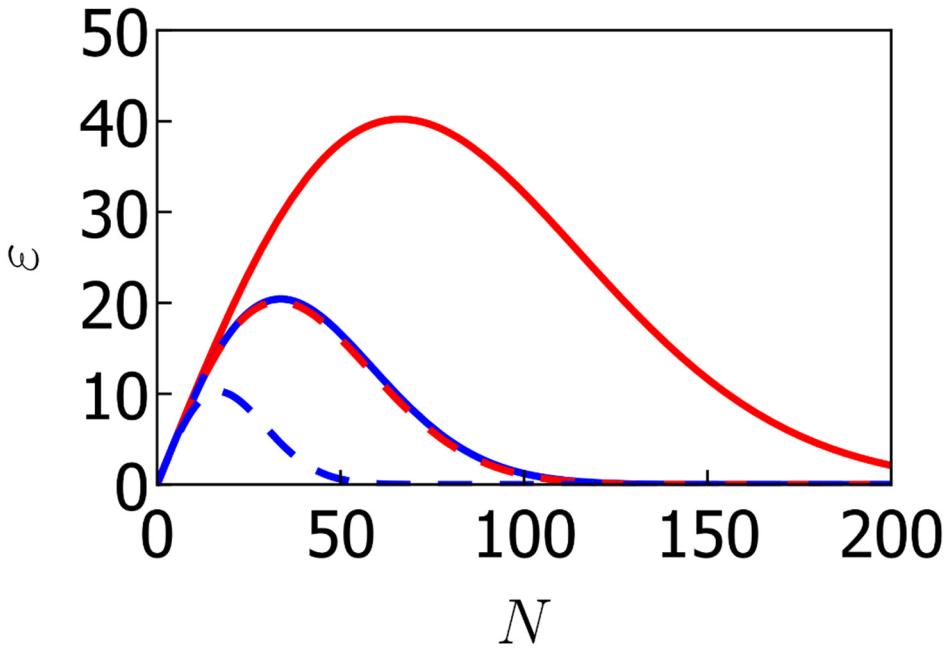

Figure 3. Improvement factor versus the momentum transfer with three different initial sizes of the atomic cloud. The final size of the atomic cloud is 1 cm. The temperature of the atoms is 6 μK. The red curves are the plots for $\sigma_0 = 0.1$ mm while the blue curves are for $\sigma_0 = 0.2$ mm. The solid (dashed) curves correspond to an angular velocity of 1 (2) μHz.

As noted earlier, even though the semi-classical model has been highly accurate in predicting the behavior of a light-pulse interferometer as well as a PSI, it is potentially useful to employ a more rigorous model that treats the center of mass motion of each atom quantum mechanically [16], since it is not evident a priori whether the semi-classical model would lead to correct predictions of observables when the point source interferometer is augmented by large momentum transfer. As such, in what follows, we present such a quantized model to augment the description of the LMT–PSI.

3. Augmented Quantum Model

The quantum state of an atom consists of its internal state and the state of its center of mass. Each atom in a PSI starts with its internal state as the ground state $|g\rangle$. We first considered the case where the center of mass of the atom is initially in a momentum eigenstate $|\boldsymbol{k}\rangle$. The evolution of the state of the center of mass is illustrated in Figure 4. The first atomic beam splitter propagating in the z-direction splits the atom into a superposition of the state $\left|\boldsymbol{k} - k^*\hat{\boldsymbol{z}}\right\rangle$ and the state $\left|\boldsymbol{k} + (k_t - k^*)\hat{\boldsymbol{z}}\right\rangle$. Here, $k_t\hat{z}$ is the difference in the momentum between the two arms, and $k^*\hat{z}$ is the common shift in the momentum for each arm. The value of k^* is zero for a conventional light-pulse atom interferometer but it has a non-zero value when the technique of LMT is employed. The value of both k_t and k^* depend on the details of the LMT process. For simplicity, we worked in a picture where the energy of the state $\left|\boldsymbol{k} - k^*\hat{\boldsymbol{z}}\right\rangle$ and the state $\left|\boldsymbol{k} + (k_t - k^*)\hat{\boldsymbol{z}}\right\rangle$ were the same and

defined as zero. The atomic mirror pulse is applied at a time T after the first atomic beam splitter. Due to the rotation perpendicular to the z-direction, the atomic mirror pulses are no longer in the original z-direction, but at an angle ΩT with respect to it. We assumed that the angular velocity of the rotation was in the x-direction, without loss of generality. For $\Omega T \ll 1$, the atomic mirror pulses turn each atom into a superposition of the state $\left|\boldsymbol{k} - k^*\hat{\boldsymbol{z}} + k_t \Omega T \hat{\boldsymbol{y}}\right\rangle \equiv |+\rangle$ and the state $\left|\boldsymbol{k} + (k_t - k^*)\hat{\boldsymbol{z}} - k_t \Omega T \hat{\boldsymbol{y}}\right\rangle \equiv |-\rangle$. The last atomic beam splitter will combine these two states approximately back to the point $\boldsymbol{k}$ in the momentum space. The Sagnac phase shift can be viewed as arising from the energy difference between the states $|+\rangle$ and $|-\rangle$. To see this, note first that the energies of these two states are no longer zero, but $\hbar^2\left[(k_t \Omega T)^2 \pm 2k_t \Omega T \boldsymbol{k}\cdot\hat{\boldsymbol{y}}\right]/2m$. Therefore, these two states oscillate at frequencies that have a difference of $2\hbar k_t \Omega T \boldsymbol{k}\cdot\hat{\boldsymbol{y}}/m$. The Sagnac phase shift is the product of this frequency difference and T, the duration for the second half of the interferometry process: $\phi = 2\hbar k_t \Omega T^2 \boldsymbol{k}\cdot\hat{\boldsymbol{y}}/m$. It can also be written as $\phi = 2\hbar\left(\boldsymbol{k}_t \times \boldsymbol{\Omega} T^2/m\right)\cdot\boldsymbol{k} \equiv \boldsymbol{r}_\Omega \cdot \boldsymbol{k}$, where $\boldsymbol{k}_t \equiv k\hat{\boldsymbol{z}}$. Note that $\boldsymbol{r}_\Omega = 2\hbar \boldsymbol{k}_\Omega T/m$, and while it has the dimension of distance, it does not represent the spatial coordinates of the center of mass of the atom. It can be shown that this expression of the phase shift is equivalent to the phase shift under the conventional description if we assign to a momentum eigenstate $\left|\boldsymbol{k}'\right\rangle$ a localized state with a velocity of $\hbar\boldsymbol{k}'/m$, determine the vectorial area $\boldsymbol{A}$ enclosed by the resulting trajectories, and use the expression $\phi = 2m\,\boldsymbol{\Omega}\cdot\boldsymbol{A}/\hbar$.

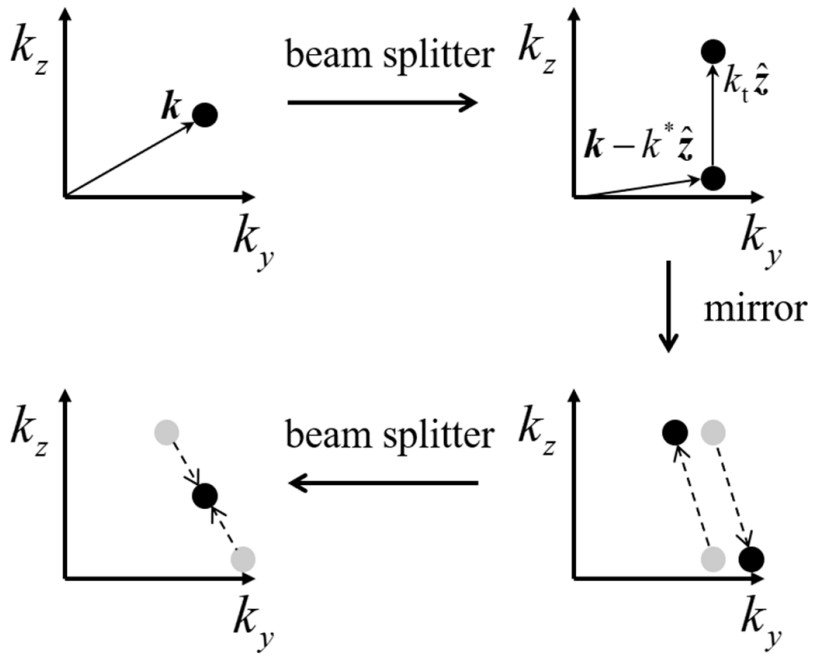

Figure 4. The evolution of a momentum eigenstate $|\boldsymbol{k}\rangle$ in the $k-$space in a PSI under rotation. A $k-$eigenstate is a single dot in the $k-$space. The first atomic beam splitter splits $|\boldsymbol{k}\rangle$ into a superposition of two $k-$eigenstates separated by the momentum transfer $\boldsymbol{k}_t$. The atomic mirror switches the position of the two $k-$eigenstates in the absence of rotation. In the presence of rotation, however, the two $k-$eigenstates will be shifted in the k_y- direction. The second beam splitter will combine the two $k-$eigenstates and make them interfere.

Due to the rotation induced phase shift, the population of the ground state will be $\langle P_g(\boldsymbol{k})\rangle = \cos^2(\boldsymbol{r}_\Omega \cdot \boldsymbol{k}/2)$, where $P_g(k)$ is the momentum space projection operator for atoms in the ground state, defined earlier. Consequently, if initially the atoms have a continuous distribution in the momentum space, the final distribution of the ground state

population will form fringes in the momentum space. Next, we will discuss what the fringes in the momentum space mean in the coordinate space.

Here, we considered both the cases where the atoms are in a pure state and in a mixed state. If the atoms are in a pure state, then the external motion can be described by a wavefunction $\psi_k(\boldsymbol{k})$ for each atom. In the absence of rotation, the final external state of the atom internally in the ground state will be $\psi_k(\boldsymbol{k})\exp\left(-\mathrm{i}\hbar\boldsymbol{k}^2(2T)/2m\right)$. According to the preceding discussion, in the presence of rotation, the final external state of the atom internally in the ground state will be:

$$\psi'_k(\boldsymbol{k}) = \psi_k(\boldsymbol{k})\exp\left(-\mathrm{i}\hbar\frac{\boldsymbol{k}^2}{2m}2T\right)\cos(\boldsymbol{r}_\Omega\cdot\boldsymbol{k}/2) \tag{5}$$

Rearranging Equation (5) and eliminating the common phase factor, we can write:

$$\psi'_k(\boldsymbol{k}) = \frac{1}{2}\psi_k(\boldsymbol{k})\left[\exp\left(-\mathrm{i}\hbar\frac{(\boldsymbol{k}+\boldsymbol{k}_1)^2}{2m}2T\right)+\exp\left(-\mathrm{i}\hbar\frac{(\boldsymbol{k}-\boldsymbol{k}_1)^2}{2m}2T\right)\right] \tag{6}$$

where $\boldsymbol{k}_1 \equiv m\boldsymbol{r}_\Omega/4\hbar T = \boldsymbol{k}_\Omega/2$. To find the wavefunction of the atoms in the coordinate space, we computed the Fourier transform of $\psi'_k(\boldsymbol{k})$, to obtain:

$$\begin{aligned}
\psi_r(\boldsymbol{r}) &= \mathcal{F}[\psi'_k(\boldsymbol{k})]\\
&= \tfrac{1}{2}\mathcal{F}\left[\psi_k(\boldsymbol{k})\exp\left(-\mathrm{i}\hbar\tfrac{(\boldsymbol{k}+\boldsymbol{k}_1)^2}{2m}2T\right)\right]+\tfrac{1}{2}\mathcal{F}\left[\psi_k(\boldsymbol{k})\exp\left(-\mathrm{i}\hbar\tfrac{(\boldsymbol{k}-\boldsymbol{k}_1)^2}{2m}2T\right)\right]\\
&= \tfrac{1}{2}\mathcal{F}\left[\psi_k(\boldsymbol{k}-\boldsymbol{k}_1)\exp\left(-\mathrm{i}\hbar\tfrac{\boldsymbol{k}^2}{2m}2T\right)\right]\mathrm{e}^{-\mathrm{i}\boldsymbol{k}_1\cdot\boldsymbol{r}}+\tfrac{1}{2}\mathcal{F}\left[\psi_k(\boldsymbol{k}+\boldsymbol{k}_1)\exp\left(-\mathrm{i}\hbar\tfrac{\boldsymbol{k}^2}{2m}2T\right)\right]\mathrm{e}^{\mathrm{i}\boldsymbol{k}_1\cdot\boldsymbol{r}}\\
&\equiv \tfrac{1}{2}\left[\psi_-(\boldsymbol{r})\mathrm{e}^{-\mathrm{i}\boldsymbol{k}_1\cdot\boldsymbol{r}}+\psi_+(\boldsymbol{r})\mathrm{e}^{\mathrm{i}\boldsymbol{k}_1\cdot\boldsymbol{r}}\right]
\end{aligned} \tag{7}$$

where $\mathcal{F}$ stands for Fourier transform. The spatial distribution of the ground state $\langle P_g(\boldsymbol{r})\rangle = |\psi_r(\boldsymbol{r})|^2$ for an arbitrary $\psi_k(\boldsymbol{k})$ has to be calculated individually.

However, under the condition where the width of $\psi'_k(\boldsymbol{k})$ is much larger than $|\boldsymbol{k}_1|$ so that $\psi_-(\boldsymbol{r}) \approx \psi_+(\boldsymbol{r})$, both $\psi_-(\boldsymbol{r})$ and $\psi_+(\boldsymbol{r})$ will approximately equal $\mathcal{F}\left[\psi_k(\boldsymbol{k})\exp\left(-\mathrm{i}\hbar\boldsymbol{k}^2T/2m\right)\right]$, which is just the final external state of the atom internally in the ground state in the absence of rotation, as discussed before Equation (5). In that case, $\langle P_g(\boldsymbol{r})\rangle$ is simply the product of the final profile of the atom cloud and a sinusoidal function $(1+\cos\boldsymbol{k}_\Omega\cdot\boldsymbol{r})/2$. This is exactly the result predicted by the conventional model for a point source.

The condition $\psi_-(\boldsymbol{r}) \approx \psi_+(\boldsymbol{r})$, corresponding to a smaller difference between $\psi_k(\boldsymbol{k}-\boldsymbol{k}_1)$ and $\psi_k(\boldsymbol{k}+\boldsymbol{k}_1)$, yields the highest contrast in the spatial interference fringes. A state wider in the momentum space corresponds to a smaller difference between $\psi_k(\boldsymbol{k}-\boldsymbol{k}_1)$ and $\psi_k(\boldsymbol{k}+\boldsymbol{k}_1)$. This condition also corresponds to a state narrower in the position space. Therefore, for a pure state, the narrower it is in the position space, the higher the contrast is for the spatial fringes. The limiting case of narrow wavefunctions in the position space is, of course, the point source.

However, the centers of mass of all trapped atoms cannot generally be described as a pure state. According to quantum statistical mechanics, the state of the center of mass of each atom can be described by a density operator $\rho = \mathrm{e}^{-H/k_\mathrm{B}T_\mathrm{K}}$, where H is the Hamiltonian, k_B is the Boltzmann constant, and T_K is the temperature. If we assume the atoms to be non-interacting and freely moving, we have $H = (\hbar\boldsymbol{k})^2/2m$, so that the state of the center of mass of each atom is described by a density operator $\rho = \int \mathrm{d}\boldsymbol{k}\exp\left[-(\hbar\boldsymbol{k})^2/2mk_\mathrm{B}T\right]|\boldsymbol{k}\rangle\langle\boldsymbol{k}|$. This density operator lacks coherence between different momentum eigenstates because these are also the eigenstates of energy. For such a system, there will be no spatial fringes at all. To see why, we recall that, for a pure state, the width in the $k-$space determines the contrast of the spatial interference fringes. Every pure state in the density operator ρ has no width in the $k-$space. Consequently, no spatial fringe will appear. The existence of

coherence between different $|k\rangle$ states for atoms cooled by lasers have been demonstrated in experiments [17–19]. Therefore, the diagonal density matrix is inadequate, and we need a different model to describe the initial state of such cold atoms.

We considered a situation where the atoms released from a magneto-optic trap are caught in an isotropic dipole force trap before the onset of the PSI process. Such a trap can be modeled as a harmonic potential well [20] with a characteristic frequency ω, so that the Hamiltonian can be expressed as:

$$H = \frac{(\hbar \boldsymbol{k})^2}{2m} + \frac{1}{2} m\omega^2 \boldsymbol{x}^2 \tag{8}$$

The energy eigenstates of this Hamiltonian are:

$$|n\rangle = \frac{a}{\sqrt{\pi^{1/2} 2^n n!}} \int \mathrm{d}\boldsymbol{k} \mathrm{H}_n(ka) \mathrm{e}^{-(ka)^2/2} |\boldsymbol{k}\rangle \tag{9}$$

where $a = \sqrt{\hbar/m\omega}$ is a measure of the size of the trap and H_n is the n-th order Hermite polynomial. The density operator of the atoms in this case can be expressed as:

$$\rho = \sum_{n=0}^{\infty} \exp\left[-\frac{\hbar\omega(n+1/2)}{k_\mathrm{B} T_\mathrm{K}}\right] |n\rangle\langle n| \tag{10}$$

During the expansion of the atom cloud, upon release from the trap, each $|n, g\rangle$ (defined as the state where the external state is $|n\rangle$ and the internal state is $|g\rangle$) evolves independently. The evolution of each $|n, g\rangle$ under the sequence of pulses used for the PSI can also be evaluated individually. We defined as $\psi_n(\boldsymbol{k})$ the final external state corresponding to $|n, g\rangle$, for an atom in the ground state internally. The signal at the end of the PSI process can thus be expressed as:

$$\langle P_g(\boldsymbol{k}) \rangle = \mathrm{tr}\left(\rho P_g(\boldsymbol{k})\right) = \sum_{n=0}^{\infty} \exp\left[-\frac{\hbar\omega(n+1/2)}{k_\mathrm{B} T_\mathrm{K}}\right] |\psi_n(\boldsymbol{k})|^2 \tag{11}$$

where $P_g(\boldsymbol{k})$ is the momentum space projection operator for atoms in the ground state, as defined earlier. Equation (11) shows that the overall contrast is determined by the sum of the fringes resulting from each energy eigenstate, $|n, g\rangle$. Therefore, the smaller a is, the narrower all the energy eigenstates will be in the position space, and the higher the contrast of the spatial fringes will be.

In Figure 5, we show a comparison between the signal of the PSI for two different values of a. For simplicity, we have considered here the case where the rotation is around the y-axis only, so that fringes occur only in the x-direction. For both curves, the temperature of the atoms was $T_\mathrm{K} = 0.1$ nK, and the half expansion time $T = 10$ s. The rotation rate wavenumber used was $k_\Omega = 2\pi \times 10\ \mathrm{cm}^{-1}$. The red curve shows the case where $a = 0.002$ cm, and the blue curve shows the case where $a = 0.004$ cm. We can see that with a smaller a, the contrast of the interference fringes was higher, as expected. In the simulation, we assumed that the sum in Equation (11) was truncated at a maximum occupation number, n_{max}, for the harmonic oscillator. This occupation number is dictated by the parameter $\alpha \equiv k_\mathrm{B} T_\mathrm{K}/\hbar\omega$. Specifically, the sum in Equation (11) was carried out from $n = 0$ to $n_{max} = 4\alpha$ and rounded to the nearest integer, which is sufficient to ensure that contributions from the excluded terms (i.e., for terms with $n > 4\alpha$) were negligible. For the red curve, we had $\alpha = 7.2$ and for the blue curve $\alpha = 28.9$.

To show the relationship between the augmented quantum model and the semi-classical model, we considered the artificial case of a one-dimensional harmonic oscillator along the x direction. The starting point was the density of atoms along the x-direction at the onset of the PSI process. Since all the atoms were assumed to be in the ground internal

state, this density distribution for the augmented quantum model can be determined from the density operator in Equation (10) as follows:

$$\langle P_g(x)\rangle = \mathrm{tr}\left(\rho P_g(x)\right) = \sum_{n=0}^{\infty} \exp\left[-\frac{\hbar\omega(n+1/2)}{k_B T_K}\right] |\phi_n(x)|^2 \tag{12}$$

where $P_g(x) \equiv |g,x\rangle\langle g,x|$ is the projection operator for atoms in the ground state, and $\phi_n(x)$ is the Hermite–Gaussian spatial wavefunction for the n-th eigenstate of the harmonic oscillator. The corresponding density distribution according to the semi-classical model and classical statistical mechanics can be expressed as:

$$\langle P_g(x)\rangle \equiv n_0(x) = \exp\left(-m\omega^2 x^2/2k_B T_K\right) \equiv \exp\left(-x^2/2\sigma_0^2\right) \tag{13}$$

It then follows that the initial cloud size parameter σ_0 in the semi-classical model is related to ω according to the expression $\sigma_0 = \sqrt{k_B T_K/m\omega^2}$. We recalled that the harmonic oscillator scale parameter a in the augmented quantum model was related to ω according to the expression $a = \sqrt{\hbar/m\omega}$. Thus, we see that $(\sigma_o/a)^2 = k_B T_K/\hbar\omega = \alpha$. At a first glance, it may not at all be obvious how the augmented quantum model density distribution as given by Equation (12) is related to the semi-classical density distribution as given by Equation (13). However, it turns out that for a highly thermal case, corresponding to $\alpha \gg 1$, these two distributions are essentially identical. This is not surprising, since a highly thermal system generally behaves in a manner similar to what is expected classically.

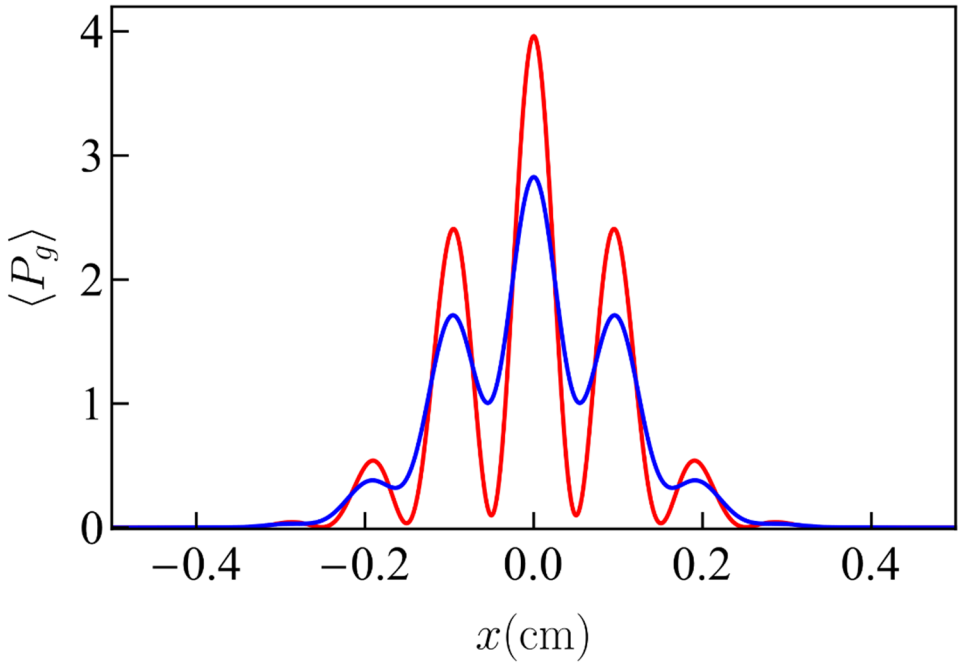

Figure 5. Comparison of signal fringes for two different values of the initial size, a. The red (blue) curve shows the case where a = 0.002 (0.004) cm. As can be seen, the contrast of the signal fringes is higher for smaller initial sizes. The rotation rate wavenumber used is $k_\Omega = 2\pi \times 10\ \mathrm{cm}^{-1}$.

We illustrate this correspondence in the top panel of Figure 6. In Figure 6a, we show plots of this density distribution using the expressions from both the augmented quantum model (red) of Equation (12) and the semi-classical model (dashed blue) of Equation (13). The parameters used were $\sigma_0 = 0.1$ mm, α = 10 and $n_{\max}$ = 40. The plots are almost identical, and the difference is hard to infer from these plots. As such, in Figure 6b, we have shown in the blue curve the difference between the density distribution for the augmented quantum model and the semi-classical model for the plots shown in Figure 6a. In the

red curve in Figure 6b, we have shown the corresponding difference when $\alpha = 20$ and $n_{\max} = 80$, with the value of σ_0 unchanged. Thus, we see that this difference, while small, is real, and did not tend to vanish as the value of α increased.

Next, we considered the PSI interaction. The fringes produced by the augmented quantum model (red) and the semi-classical model (dashed blue) are shown in Figure 6c. The parameters used here were $\sigma_0 = 0.1$ mm, $\sigma_f = 1$ mm, $\alpha = 10$, $n_{\max} = 40$, and $k_\Omega = 2\pi \times 10$ cm^{-1}. Again, the plots are almost identical, and the difference is hard to infer from these plots. As such, in Figure 6d, we have shown in the blue curve the difference between the density distribution for the augmented quantum model and the semi-classical model for the plots shown in Figure 6c. In the red curve in Figure 6d, we have shown the corresponding difference when $\alpha = 20$ and $n_{\max} = 80$, with the value of σ_0 and σ_f unchanged. Again, we see that the difference, while small, is real, and does not tend to vanish as the value of α is increased.

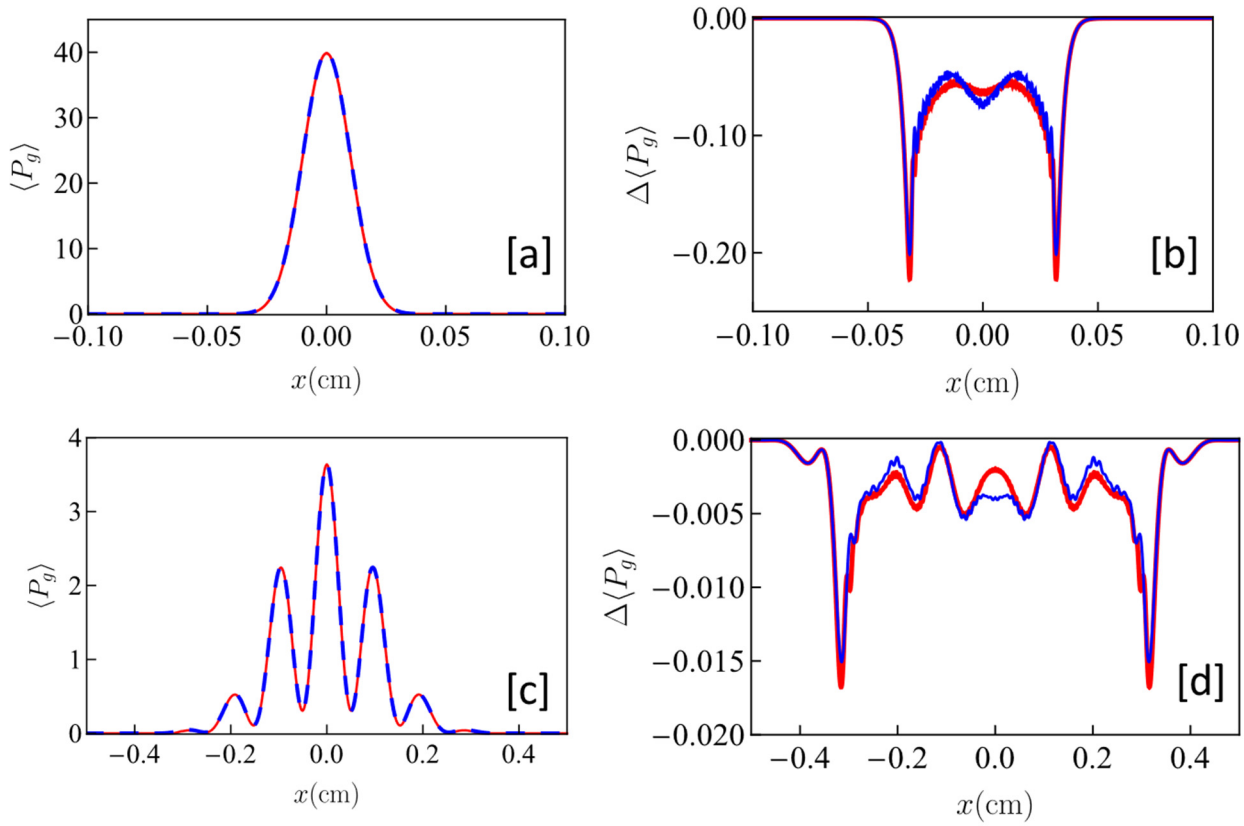

Figure 6. (**a**) Comparison of the initial density distributions according to the augmented quantum model (red) and the semi-classical model (dashed blue), for $\sigma_0 = 0.1$ mm, $\alpha = 10$ and $n_{\max} = 40$; this serves as the initial state of the PSI. (**b**) The difference between the density distributions due to the augmented quantum model and the semi-classical model for $\alpha = 10$ and $n_{\max} = 40$ (blue) and $\alpha = 20$ and $n_{\max} = 80$ (red); (**c**) Comparison of the PSI signals computed using the augmented quantum model (red) and the semi-classical model (dashed blue) for are $\sigma_0 = 0.1$ mm. $\sigma_f = 1$ mm, $\alpha = 10$, $n_{\max} = 40$ and $k_\Omega = 2\pi \times 10$ cm^{-1}; (**d**) The difference between the PSI signals for the augmented quantum model and the semi-classical model, for $\alpha = 10$ and $n_{\max} = 40$ (blue) and $\alpha = 20$ and $n_{\max} = 80$ (red).

We recall that, according to the Ehrenfest theorem, the behavior of the quantum mechanical expectation values of the position and the momentum of a particle are identical to their classical values if the Hamiltonian is at most quadratic in position as well as momentum. The condition for the Ehrenfest theorem is satisfied for free space propagation, as well as the Sagnac effect, which is modeled here as a simple rotation in the coordinate system. On the other hand, the Hamiltonian representing the interaction with the light fields for the PSI considered in Figure 6, has a spatial dependence of the form $\exp(ik_t z)$, which is not consistent with the requirement of the Ehrenfest theorem. However, in the

semi-classical model, the effect of such a Hamiltonian is considered *quantum mechanically* (rather than classically), in assigning a momentum difference of $\hbar k_t$ between the two arms. As such, it is reasonable to conclude that the difference in the signals for the PSI computed by these two models differ due to the difference in the initial density distributions only.

To summarize, for highly thermal atoms ($k_B T_K \gg \hbar\omega$) released from a harmonic oscillator trap, the PSI signals predicted by the augmented quantum model would be very similar to, although not exactly the same as, those predicted by the semi-classical model. However, if $k_B T_K \sim \hbar\omega$, this convergence of results will not occur. The extreme example is the Bose-Einstein Condensate (BEC). The pure case considered above in fact corresponds to the BEC (with the order parameter behaving as the single particle wavefunction) in the ideal limit where the scattering length vanishes and there is no interaction among the atoms [21]. As we have shown above, the PSI signal in that case would be the same as that predicted for an ideal, point-source based PSI employing the semi-classical model, but only in the limit where the initial momentum spread is much larger than k_Ω. For the realistic cases where the scattering length does not vanish, the augmented quantum model would be more complicated due to non-linearity; such an analysis is beyond the scope of this paper. Furthermore, it is not clear whether there is an effective semi-classical model for a BEC, especially in this non-linear regime.

4. Large Momentum Transfer by Additional Raman Pulses

Large momentum transfer (LMT) atom optics are broadly defined as methods that increase the momentum splitting between the interferometer arms beyond $2\hbar k$. In light-pulse atom interferometry, several LMT techniques have been demonstrated. These include using an additional sequence of π pulses [4,5,22–26] or Bloch oscillations in an optical lattice [27–30] following the initial $\pi/2$ pulse to increase the momentum splitting, as well as implementing individual $\pi/2$ pulses that transfer an increased number of photon momentum recoils via higher order Bragg diffraction [31]. For the sequential pulse method, either Raman transitions [15], which change the internal hyperfine state, or Bragg transitions [4,5,18,19], which leave the internal state unchanged, can be used. Both methods have their advantages and are worth considering for a given application. For instance, Raman transitions are capable of efficiently transferring atom clouds with wider velocity spreads along the laser beam axis [23], while Bragg transitions are immune to sources of noise or drift arising from effects involving a changing internal state, such as ac Stark shifts of the transition resonance [7,16,24,32]. Bloch oscillations also have the advantage of a very high momentum transfer efficiency that is robust against intensity inhomogeneities across the atom cloud [20–23]. Sequences of single-photon transitions on the 689 nm inter-combination transition of strontium [33] represent an alternative approach that offers wide velocity acceptance and reduced AC Stark shifts. This promising approach will be studied in future work. We also note that another technique for large momentum transfer is the so-called echo atom interferometry [34]. However, this type of interferometer is not well-suited for rotation sensing since the interference signal results from many different paths simultaneously. As such, this approach for large momentum transfer does not seem to have direct relevance in enhancing the rotation measurement sensitivity of a PSI. An evaluation of echo interferometry for rotation sensing would require further study.

Techniques such as Bragg diffraction and Bloch oscillation in optical lattices require atoms with sub-recoil velocity spreads in the longitudinal direction, requiring either velocity selection or increased cooling, which adversely affect the signal to noise ratio as well as the repetition rate. As such, we focus here on the method of using additional Raman pulses [15–17]. The protocol for realizing LMT using this method is illustrated in Figure 7. Additional Raman pulses in alternating directions are added to the conventional $\pi/2 - \pi - \pi/2$ pulse sequence.

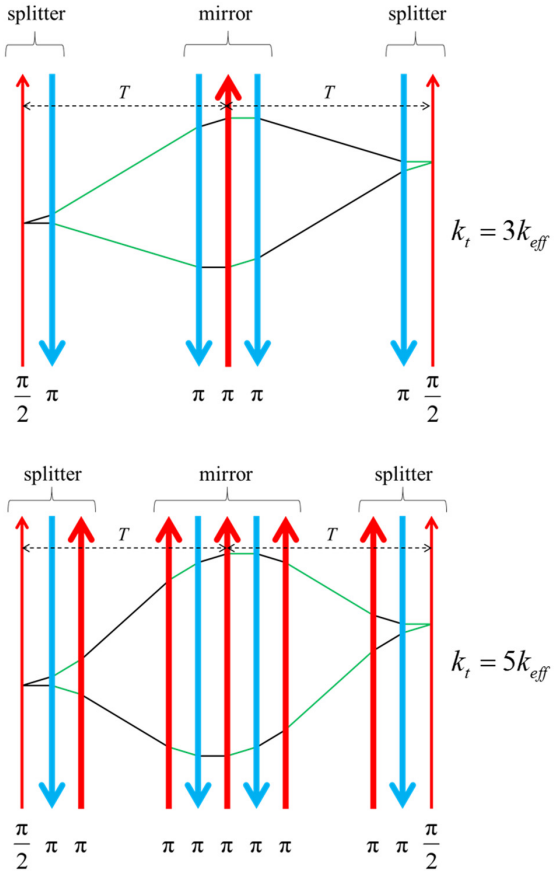

Figure 7. Large momentum transfer by additional $\pi-$pulses in alternating directions. Each Raman pulse here is a pair of counterproparating Raman beams. The arrows show the effective directions of Raman pulses.

The modeling of the motion of the center of mass of each atom was discussed earlier in Section 3. Here, we describe the evolution of the internal states of each atom under this Raman pulse sequence. The internal state is modeled as a three-level system: the ground state $|g\rangle$, the excited state $|e\rangle$, and the intermediate state $|i\rangle$. The pulses induce Raman transitions among these three states. The frequency and the wavenumber of the first (second) Raman beam are denoted as ω_1 (ω_2) and $\boldsymbol{k}_1$ ($\boldsymbol{k}_2$). Due to conservation of linear momentum, a pair of Raman beams couples the three states $|g, \boldsymbol{k}\rangle$, $|i, \boldsymbol{k} + \boldsymbol{k}_1\rangle$, and $|e, \boldsymbol{k} + \boldsymbol{k}_1 - \boldsymbol{k}_2\rangle$. The resulting Hamiltonian, in the basis spanned by these three states, can be expressed as follows:

$$H_{\text{Raman}} = \hbar \begin{bmatrix} \frac{\hbar k^2}{2m} + \frac{\delta_0}{2} & \frac{\Omega_1}{2} & 0 \\ \frac{\Omega_1}{2} & \frac{\hbar(\boldsymbol{k}+\boldsymbol{k}_1)^2}{2m} - \Delta_0 & \frac{\Omega_2}{2} \\ 0 & \frac{\Omega_2}{2} & \frac{\hbar(\boldsymbol{k}+\boldsymbol{k}_1-\boldsymbol{k}_2)^2}{2m} - \frac{\delta_0}{2} \end{bmatrix} \tag{14}$$

where $\delta_0 = \delta_{g0} - \delta_{e0}$ and $\Delta_0 = \left(\delta_{g0} + \delta_{e0}\right)/2$. Here, δ_{g0} is defined as $\omega_1 - \left(\omega_i - \omega_g\right)$ and δ_{e0} as $\omega_2 - \left(\omega_i - \omega_e\right)$. With the adiabatic elimination [35], we obtain the effective two-level system Hamiltonian, in the basis spanned by states $|g, \boldsymbol{k}\rangle$ and $|e, \boldsymbol{k} + \boldsymbol{k}_1 - \boldsymbol{k}_2\rangle$:

$$H = \begin{bmatrix} \frac{\hbar \boldsymbol{k}^2}{2m} + \frac{\delta_0}{2} - \frac{\Omega_1^2}{2\left[\frac{\hbar(\boldsymbol{k}+\boldsymbol{k}_1)^2}{m} - 2\Delta_0\right]} & \frac{-\Omega_1\Omega_2}{2\left[\frac{\hbar(\boldsymbol{k}+\boldsymbol{k}_1)^2}{m} - 2\Delta_0\right]} \\ \frac{-\Omega_1\Omega_2}{2\left[\frac{\hbar(\boldsymbol{k}+\boldsymbol{k}_1)^2}{m} - 2\Delta_0\right]} & \frac{\hbar(\boldsymbol{k}+\boldsymbol{k}_1-\boldsymbol{k}_2)^2}{2m} - \frac{\delta_0}{2} - \frac{\Omega_2^2}{2\left[\frac{\hbar(\boldsymbol{k}+\boldsymbol{k}_1)^2}{m} - 2\Delta_0\right]} \end{bmatrix} \tag{15}$$

If we set $\delta_0 = \hbar(\boldsymbol{k}_1 - \boldsymbol{k}_2)^2/2m$, $\Omega_1 = \Omega_2 \equiv \Omega_0$, and shift all energy levels by an amount that makes the energy of state $|g, \boldsymbol{k}\rangle$ vanish, we have:

$$H = \hbar \begin{bmatrix} 0 & \frac{\Omega_0^2}{4\widetilde{\Delta}_0} \\ \frac{\Omega_0^2}{4\widetilde{\Delta}_0} & \frac{\hbar \boldsymbol{k}\cdot(\boldsymbol{k}_1 - \boldsymbol{k}_2)}{m} \end{bmatrix} \tag{16}$$

where $\widetilde{\Delta}_0 \equiv \left[\Delta_0 - \hbar(\boldsymbol{k} + \boldsymbol{k}_1)^2/2m\right]$. From this Hamiltonian we see a detuning caused by the Doppler shift given by $\hbar\boldsymbol{k} \cdot (\boldsymbol{k}_1 - \boldsymbol{k}_2)/m$, as well as the effective Rabi frequency given by $\Omega_0^2/2\widetilde{\Delta}_0$. In addition, the adiabatic elimination also gives us the effective decay rate [28] between the states $|g\rangle$ and $|e\rangle$:

$$\Gamma_{g\to e}^{\text{eff}} = \frac{\Gamma_{i\to e}\Omega_0^2}{4\widetilde{\Delta}_0^2};\ \Gamma_{e\to g}^{\text{eff}} = \frac{\Gamma_{i\to g}\Omega_0^2}{4\widetilde{\Delta}_0^2} \tag{17}$$

The total decay rate for the coherence between states $|g\rangle$ and $|e\rangle$ is then given by:

$$\Gamma_{\text{eff}} = \Gamma_{g\to e}^{\text{eff}} + \Gamma_{e\to g}^{\text{eff}} = \frac{\Gamma\Omega_0^2}{4\widetilde{\Delta}_0^2} \tag{18}$$

The D_2 line decay rate from $5^2P_{3/2}$ to $5^2S_{1/2}$, expressed as $\Gamma = \Gamma_{i\to g} + \Gamma_{i\to e}$, is about $2\pi \times$ (6 MHz) for ^{87}Rb. Only the atoms that have not experienced spontaneous emission keep their phase information. The fraction of atoms that have decohered by the end of the interferometry process is given by $\exp(-\Gamma_{\text{eff}}\tau)$, where τ is the total duration of all the Raman pulses. With this model, we can simulate the signal for a PSI–LMT, while taking into account the complexities caused by detuning. The effect of spontaneous emission is considered later in a heuristic manner. In the model discussed in Section 3, we assumed all $k-$components to be resonant, which is approximately valid if the effective Rabi frequency is much larger than the Doppler shift. In order to account for more general conditions, in our simulation we used different Hamiltonian operators for different $k-$components, corresponding to Equation (16).

The computation process for determining the PSI signal can be summarized as follows. As we illustrated before, each pure state in Equation (10) evolves independently. Therefore, we can calculate the evolution of each pure state and add them up according to the initial weight in the end. In each pure state, consider a single point in the k-space as an example of the simulation. The state $|g, \boldsymbol{k}\rangle$ will see the first $\pi/2$ pulse dictated by the Hamiltonian in Equation (16), and become a superposition of a point (in the k-space) of the ground state and a point (in the k-space) of the excited state. Then they evolve freely for time T. The free evolution is dictated by the Hamiltonian in Equation (16) with $\Omega_0 = 0$. Then they see the π pulse also dictated by Equation (16). The beams of the π-pulse are rotated by the angle ΩT (where Ω is the rate of rotation). The π-pulse is imperfect due to the Doppler shift detuning, resulting in a state that is a superposition of two points (in the k-space) of the ground state and two points (in the k-space) of the excited state. After another free evolution of T, they see the final $\pi/2$-pulse and become a superposition of four points (in the k-space) of the ground states and four points (in the k-space) of the excited states. With the final state in the k-space, we can calculate the state in the position space.

Using this approach, we simulated the signals for the case of atoms released from a harmonic oscillator trap, as shown in Equation (10), for ^{87}Rb, with the following parameters: $\Omega_0 = 2\pi \times \left(10\sqrt{10}\,\text{MHz}\right)$, $\Delta_0 = 2\pi \times (500\,\text{MHz})$, $T_{\text{K}} = 6\,\mu\text{K}$, and $a = 0.1\,\mu\text{m}$. Here, we chose an unrealistically small size of the trap, in order to elucidate the behavior of a system that is very close to an ideal point source. The simulation results for this case are shown in Figure 8. The main difference from the result shown in Figure 2 is that the height of the signal peak is shorter since the detuning resulting from k_{t} (the difference in the momentum in the z-direction between the two arms, as defined earlier in Section 2) was taken into

account. There is also a little difference in the width of the signal peak. For the LMT case shown in panel B, there are also some small peaks in addition to the main signal peak. This is because the pulses are not ideal. For example, a pulse that is nominally designated to be a π-pulse does not fully transform a ground state to an excited state, or vice versa, but will leave some residual. The small peaks are the consequence of the interference involving the residuals.

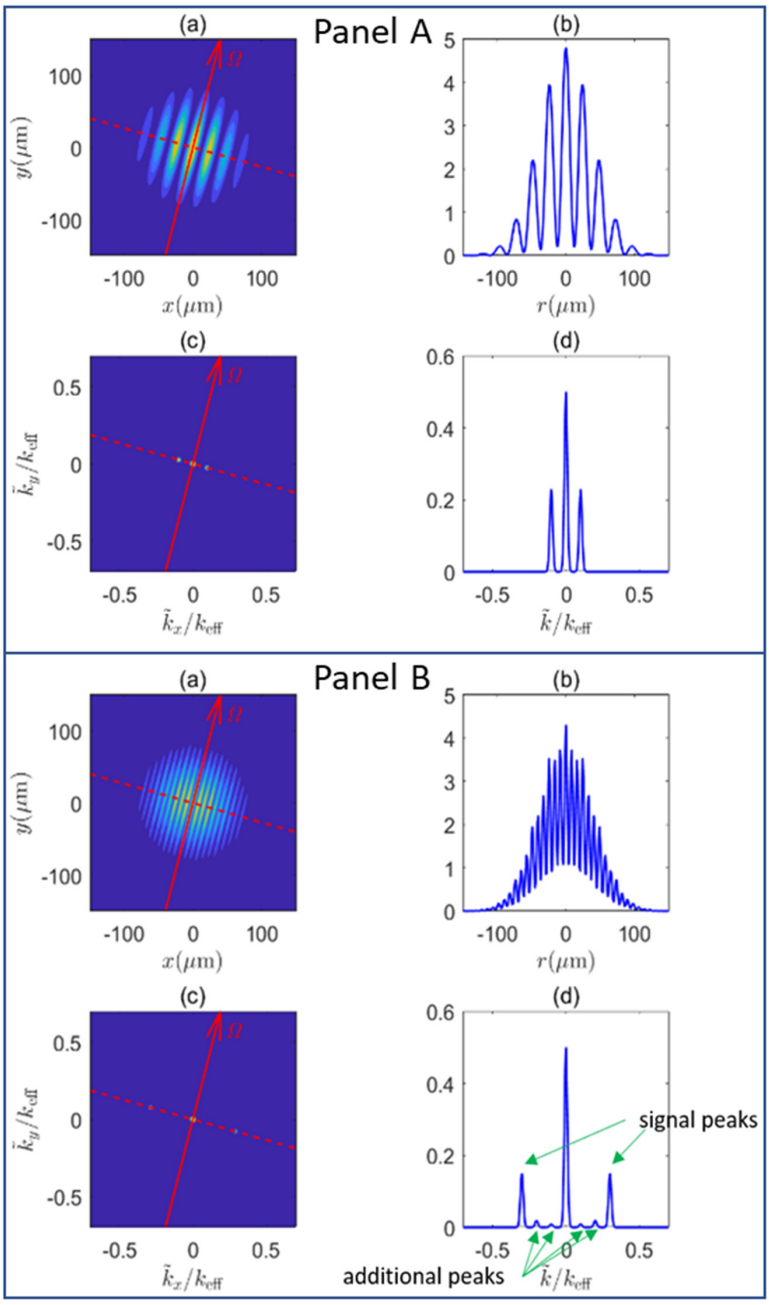

Figure 8. Simulation results for the conventional PSI (**Panel A**: $k_{\rm t} = k_{\rm eff}$) and the LMT–PSI (**Panel B**: $k_{\rm t} = 3k_{\rm eff}$) employing ^{87}Rb with the parameters $\Omega_0 = 2\pi \times \left(10\sqrt{10}\ \text{MHz}\right)$, $\Delta_0 = 2\pi \times (500\ \text{MHz})$, $T_{\rm K} = 6\ \mu\text{K}$, and $a = 0.1\ \mu\text{m}$, including the detuning effect. In each panel, (**a**) is the plot of $\langle P_g(\boldsymbol{r})\rangle$ in the plane perpendicular to $\boldsymbol{k}_{\rm t}$, (**b**) is the cross section at the dashed line in (**a**), (**c**) is the plot of $\widetilde{P}_g\left(\tilde{\boldsymbol{k}}\right)$ in the plane perpendicular to $\boldsymbol{k}_{\rm t}$, and (**d**) is the cross section at the dashed line of (**c**). The orientation of the signal indicates the direction of the angular velocity.

As can be seen from comparisons between the PSI and LMT–PSI results shown in Figure 8, the LMT process produces a larger separation for the signal peaks in the Fourier transform domain, thus making it more sensitive for measuring rotation. At the same time, the amplitudes of the signal peaks are smaller, which in turn would represent a reduction in the effective signal to noise ratio, and a corresponding reduction in sensitivity. The actual improvement in sensitivity would be determined by both factors. In this context, we consider first the fact that the degradation of the signal (both in terms of the reduction in the amplitudes, and the appearance of additional peaks) can be countered by increasing the effective Rabi frequency: $\Omega_0^2/2\Delta_0$. As we mentioned before, the maximum heights for the signal peaks occur when $\Omega_0^2/2\Delta_0 \to \infty$. Figure 9 shows the comparison between signals for different effective Rabi frequencies, with $k_t = 3k_{\text{eff}}$. Panel A in Figure 9 corresponds to the case where $\Omega_0 = 2\pi \times \left(10\sqrt{10}\,\text{MHz}\right)$ and $\Delta_0 = 2\pi \times (500\,\text{MHz})$. Panel B (which is the same as Panel A of Figure 8) corresponds to the case where $\Omega_0 = 2\pi \times (100\,\text{MHz})$ and $\Delta_0 = 2\pi \times (500\,\text{MHz})$. As can be seen, the amplitudes of the signal peaks increase for the larger value of the effective Rabi frequency, and the additional peaks almost disappear completely. Figure 10 shows a signal for $k_t = 7k_{\text{eff}}$ with $\Omega_0 = 2\pi \times (100\,\text{MHz})$ and $\Delta_0 = 2\pi \times (500\,\text{MHz})$. We can see in this case that the signal is still very close to the ideal signal that does not take into account the effect of detuning. Simulations with larger k_t require extremely large amounts of computational resources because we used a fully quantum model. Attempts will be made in the near future to extend the simulation to much larger values of k_t. In what follows, we present a systematic analysis for estimating quantitatively the expected net enhancement in sensitivity as a function of the effective Rabi frequency and the value of k_t, while taking into account the effect of spontaneous emission heuristically.

Before proceeding with this analysis, we note for clarity that the results presented in Figures 8–10 have been computed with the augmented quantum model. However, if the semi-classical model were used instead, the results would be very similar, even when the Doppler detuning is taken into account, with the difference being very small of the order of what is shown in Figure 6d. Furthermore, as noted above, carrying out the analysis with the augmented quantum model for a significant value of N requires enormous computational resources. Given that the difference between the results produced by the semi-classical analysis and the augmented quantum model is very small, undertaking such an analysis was not deemed critically important at this point. Instead, in order to estimate the degree of enhancement achievable using LMT for increasing values of N, in what follows we make a simplifying assumption that eliminates the distinction between the augmented quantum model and the semi-classical model. Specifically, in the estimation of the contrast of the fringes (equivalently, the height of the signal peak in the Fourier transform domain) we ignore the momentum distribution of the atoms and assume that all atoms see the same detuning. Therefore, the effect of the Doppler shift detuning will produce only an overall reduction in the signal peak. Consequently, the quantized model for the motion of the center of mass of the atoms becomes irrelevant. The spontaneous emission also only results in an overall reduction in the signal peak, and thus does not depend on the quantized model for the motion of the center of mass of the atoms. As such, the rest of the results that follow in this section are based on the semi-classical model.

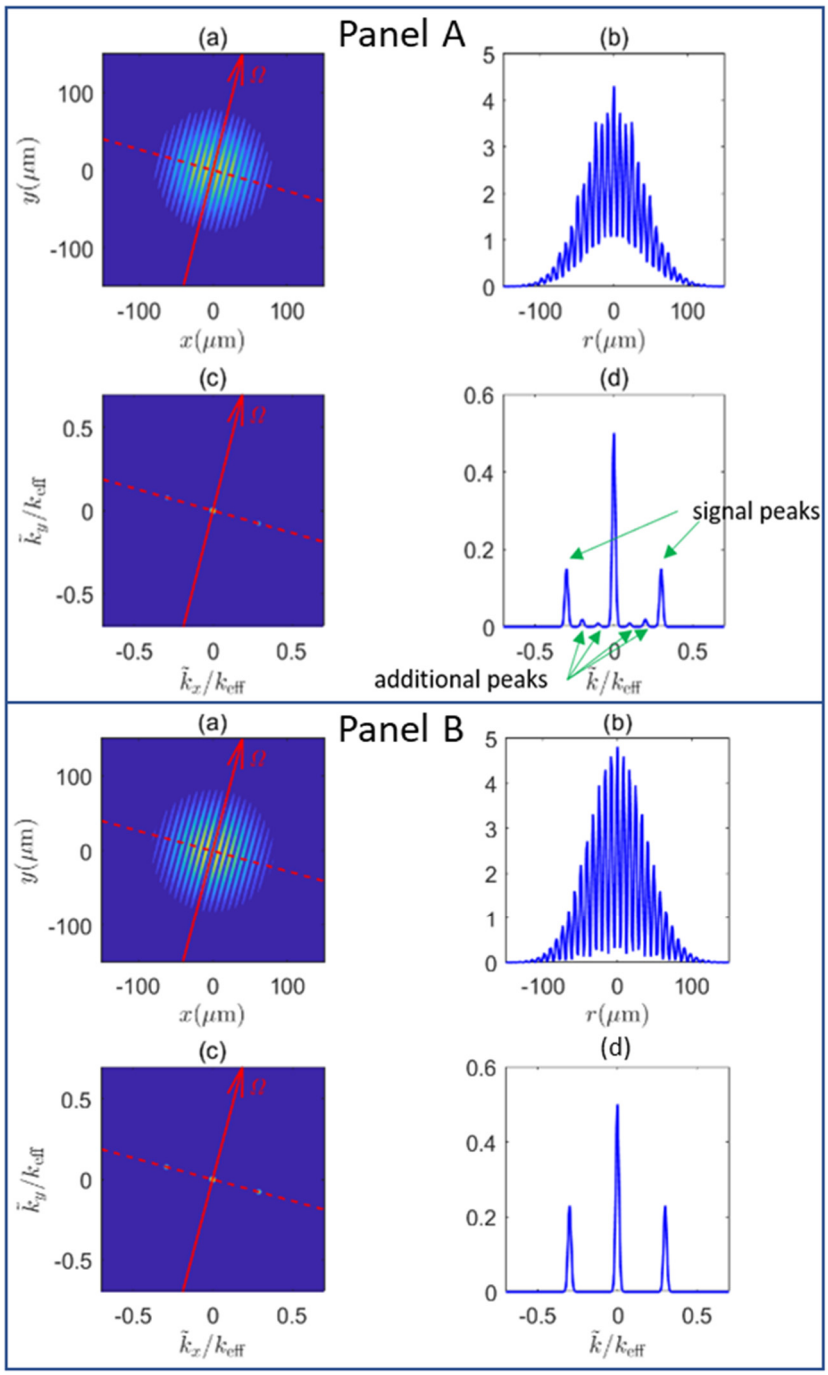

Figure 9. Comparison between the signals with low and high effective Rabi frequencies, with $k_t = 3k_{eff}$, $T_K = 6$ μK, and $a = 0.1$ μm. **Panel A** corresponds to the case where $\Omega_0 = 2\pi \times \left(10\sqrt{10}\,\text{MHz}\right)$ and $\Delta_0 = 2\pi \times (500\,\text{MHz})$. **Panel B** corresponds to the case where $\Omega_0 = 2\pi \times (100\,\text{MHz})$ and $\Delta_0 = 2\pi \times (500\,\text{MHz})$. In each panel, (**a**) is the plot of $\langle P_g(\boldsymbol{r})\rangle$ in the plane perpendicular to $\boldsymbol{k}_t$, (**b**) is the cross section at the dashed line in (**a**), (**c**) is the plot of $\widetilde{P}_g\left(\tilde{\boldsymbol{k}}\right)$ in the plane perpendicular to $\boldsymbol{k}_t$, and (**d**) is the cross section at the dashed line of (**c**). With the higher effective Rabi frequency, the contrast of the signal is improved significantly. Note that the plot in **Panel A** here is identical to the plot in **Panel B** of Figure 8.

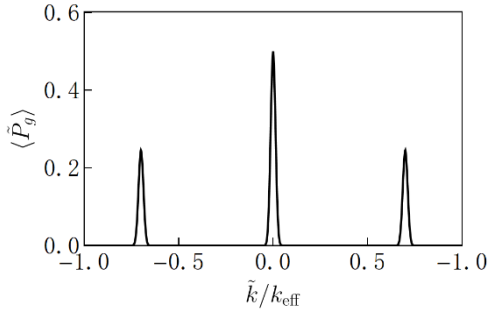

Figure 10. The signal for $k_t = 7k_{\text{eff}}$ with $\Omega_0 = 2\pi \times (100\ \text{MHz})$ and $\Delta_0 = 2\pi \times (500\ \text{MHz})$. This is to be compared with graph (d) in Panel B of Figure 9, with the only difference being in the value of k_t. In this case, the signal is still very close to the ideal one that does not take into account the effect of detuning, meaning that such parameters work fine for a momentum transfer of $7k_{\text{eff}}$. This is the largest momentum transfer we have rigorously simulated so far.

The value of h, the height of the signal peaks in the Fourier transform domain, defined earlier in Section 2, is determined primarily by the transition efficiency of each $\pi-$ pulse and the effective spontaneous emission. To simplify the analysis, as noted above, we ignore the dependence of the effective Rabi frequency on the momentum of the atoms. Therefore, we define the constant effective Rabi frequency as $\Omega_{\text{eff}} \equiv \Omega_0^2/2\Delta_0$. We define the propagator of the quantum state of the atom due to a Raman pulse, U, by the expression $|\psi(t_0 + t)\rangle = U(t)|\psi(t_0)\rangle$. This propagator including the effect of detuning caused by the Doppler shift can be expressed as:

$$U(t) = \begin{bmatrix} \cos\frac{\Omega' t}{2} - \mathrm{i}\frac{\delta}{\Omega'}\sin\frac{\Omega' t}{2} & -\mathrm{i}\frac{\Omega_{\text{eff}}}{\Omega'}\sin\frac{\Omega' t}{2} \\ -\mathrm{i}\frac{\Omega_{\text{eff}}}{\Omega'}\sin\frac{\Omega' t}{2} & \cos\frac{\Omega' t}{2} - \mathrm{i}\frac{\delta}{\Omega'}\sin\frac{\Omega' t}{2} \end{bmatrix} \tag{19}$$

where $\Omega' \equiv \sqrt{\Omega_{\text{eff}}^2 + \delta^2}$ and δ is the detuning caused by the Doppler shift. In principle, even the atoms following the same trajectories will have a thermal distribution of momenta. However, in the LMT case with N much larger than unity, the thermal momentum is very small compared to k_t. With $T_K = 6\ \mu\text{K}$, the typical thermal momentum, $\sqrt{mk_B T_K}$, is only ~$2\hbar k_{\text{eff}}$. Therefore, we ignore the thermal momentum distribution of the atoms, which means that atoms following the same trajectories experience the same detuning. Generally, it is difficult to handle this propagator analytically. However, in the limit that $\delta \ll \Omega_{\text{eff}}$, we can make approximations to Equation (19) and make it more manageable. The transition efficiency of a π-pulse derived from Equation (19) is:

$$\begin{aligned} \eta_k &= \left(\frac{\Omega_{\text{eff}}}{\Omega'}\sin\frac{\Omega' t}{2}\right)^2 = \frac{1}{1+\delta_k^2/\Omega_0^2}\sin^2\frac{\mu\sqrt{1+\delta_k^2/\Omega_{\text{eff}}^2}}{2} \\ &\equiv \frac{1}{1+\beta_k}\sin^2\frac{\mu\sqrt{1+\beta_k}}{2} = \frac{1}{1+\beta_k} \end{aligned} \tag{20}$$

where $\mu \equiv \Omega_{\text{eff}} t$, δ_k is the Doppler shift inducing detuning for an atom with momentum k, and $\beta_k \equiv (\delta_k/\Omega_{\text{eff}})^2 = (\hbar k_{\text{eff}} k/m\Omega_{\text{eff}})^2$. In the last step of Equation (20), we assumed that we could make μ different for each Raman pulse, such that for all pulses $\mu_k = \pi/\sqrt{1+\beta_k}$. When $\Omega_{\text{eff}} = 2\pi \times (10\ \text{MHz})$, the value of $\beta_{100k_{\text{eff}}}$ is only ~0.1. Therefore, it is reasonable to consider β_k a small quantity. Only considering the effect of the imperfection of the π-pulses, the height of the signal peak for $k_t = Nk_{\text{eff}}$ is reduced by a factor of the multiplication of the transition efficiency of all the π-pulses times the spontaneous decay term, that is:

$$\begin{aligned} h_{Nk_{\text{eff}}} &= \tfrac{1}{4}\left(\eta_{k_{\text{eff}}}\eta_{2k_{\text{eff}}}\cdots\eta_{(N-1)k_{\text{eff}}/2}\right)^4 \exp(-\Gamma_{\text{eff}}\tau) \\ &= \frac{1}{4\left[\left(1+\beta_{k_{\text{eff}}}\right)\left(1+\beta_{2k_{\text{eff}}}\right)\cdots\left(1+\beta_{(N-1)k_{\text{eff}}/2}\right)\right]^4} \\ &\exp\left(-\Gamma_{\text{eff}}\frac{\pi}{\Omega_{\text{eff}}}4\left(\frac{1}{\sqrt{1+\beta_{k_{\text{eff}}}}}+\frac{1}{\sqrt{1+\beta_{2k_{\text{eff}}}}}+\cdots\frac{1}{\sqrt{1+\beta_{(N-1)k_{\text{eff}}/2}}}\right)\right) \end{aligned} \tag{21}$$

Then the logarithm of the height is:

$$\ln h_{Nk_{\text{eff}}} = -4\sum_{n=1}^{(N-1)/2}\left(\ln\left(1+\beta_{nk_{\text{eff}}}\right)+\frac{\pi\Gamma_{\text{eff}}}{\Omega_{\text{eff}}\sqrt{1+\beta_{nk_{\text{eff}}}}}\right)-2\ln 2 \tag{22}$$

Keeping only the leading term of β, we have:

$$\begin{aligned} \ln h_{Nk_{\text{eff}}} &\approx -4\left(1-\tfrac{\pi\Gamma_{\text{eff}}}{2\Omega_{\text{eff}}}\right)\left(\tfrac{\hbar k_{\text{eff}}^2}{m\Omega_{\text{eff}}}\right)^2\sum_{n=1}^{(N-1)/2}n^2-\tfrac{2(N-1)\pi\Gamma_{\text{eff}}}{\Omega_{\text{eff}}}-2\ln 2 \\ &= -\tfrac{1}{6}N\left(N^2-1\right)\left(1-\tfrac{\pi\Gamma_{\text{eff}}}{2\Omega_{\text{eff}}}\right)\left(\tfrac{\hbar k_{\text{eff}}^2}{m\Omega_{\text{eff}}}\right)^2-\tfrac{2(N-1)\pi\Gamma_{\text{eff}}}{\Omega_{\text{eff}}}-2\ln 2 \\ &\approx -\tfrac{1}{6}N^3\left(1-\tfrac{\pi\Gamma_{\text{eff}}}{2\Omega_{\text{eff}}}\right)\left(\tfrac{\hbar k_{\text{eff}}^2}{m\Omega_{\text{eff}}}\right)^2-\tfrac{2\pi N\Gamma_{\text{eff}}}{\Omega_{\text{eff}}}-2\ln 2 \\ &\approx -\tfrac{1}{6}N^3\left(\tfrac{\hbar k_{\text{eff}}^2}{m\Omega_{\text{eff}}}\right)^2-\tfrac{2\pi N\Gamma_{\text{eff}}}{\Omega_{\text{eff}}}-2\ln 2 \end{aligned} \tag{23}$$

The last step in Equation (23) is valid because normally, as long as we have a reasonably large Δ_0, the value of $\pi\Gamma_{\text{eff}}/\Omega_{\text{eff}}$ is very small compared to 1. For example, if $\Omega_0 = 2\pi\times(100\,\text{MHz})$ and $\Delta_0 = 2\pi\times(500\,\text{MHz})$, we have $\pi\Gamma_{\text{eff}}/\Omega_{\text{eff}} = 0.006$. Therefore, $(1-\pi\Gamma_{\text{eff}}/2\Omega_{\text{eff}})\approx 1$. With a reasonably large Δ_0, we also note that $\Gamma_{\text{eff}} = \Gamma\Omega_0^2/4\widetilde{\Delta}_0^2 \approx \Gamma\Omega_0^2/4\Delta_0^2 = \Gamma\Omega_{\text{eff}}/2\Delta_0$. Here, we do not consider the effect of the finite initial size of the atomic cloud, so that $\varepsilon \equiv \delta\Omega_{Nk_{\text{eff}}}/\delta\Omega_{k_{\text{eff}}} = N\sqrt{h_{Nk_{\text{eff}}}/h_{k_{\text{eff}}}}$. In this expression, $h_{k_{\text{eff}}}$ can be considered the ideal height ¼, and thus $\ln h_{k_{\text{eff}}} = (-2\ln 2)$. Substituting the expressions of $h_{k_{\text{eff}}}$ and $h_{Nk_{\text{eff}}}$ into the expression of the improvement factor, we can calculate the natural logarithm of the improvement factor:

$$\ln\varepsilon = \ln N+\frac{1}{2}\ln\frac{h_{Nk_{\text{eff}}}}{h_{k_{\text{eff}}}} = \ln N-\frac{1}{3}N^3\left(\frac{\hbar k_{\text{eff}}^2\Delta_0}{m\Omega_0^2}\right)^2-\frac{\pi N\Gamma}{2\Delta_0} \tag{24}$$

The optimal value of Δ_0 for maximizing $\ln\varepsilon$ is:

$$\Delta_0^{\text{opt}} = \left(\frac{3\pi\Gamma}{4}\right)^{1/3}\left(\frac{m\Omega_0^2}{N\hbar k_{\text{eff}}^2}\right)^{2/3} \tag{25}$$

The natural logarithm of the improvement factor for this Δ_0 is:

$$\ln\varepsilon = \ln N-N^{5/3}\left(\frac{3\pi\Gamma\hbar k_{\text{eff}}^2}{4m\Omega_0^2}\right)^{2/3} \tag{26}$$

We see that the maximum value of ε is given by:

$$\varepsilon_{\max} = \mathrm{e}^{-3/5}\left(\frac{3}{125}\right)^{1/5}\left(\frac{4m\Omega_0^2}{\pi\Gamma\hbar k_{\text{eff}}^2}\right)^{2/5} = 0.56\left[\frac{\Omega_0}{2\pi\times(1\,\text{MHz})}\right]^{4/5} \tag{27}$$

This value of ε occurs for an optimal value of N, given by:

$$N_{\text{opt}} = \left(\frac{3}{125}\right)^{1/5}\left(\frac{4m\Omega_0^2}{\pi\Gamma\hbar k_{\text{eff}}^2}\right)^{2/5} = 1.0\left[\frac{\Omega_0}{2\pi\times(1\text{ MHz})}\right]^{4/5} \tag{28}$$

We can see from Equations (27) and (28) that both ε_{max} and N_{opt} are proportional to $\Omega_0^{4/5}$. Figure 11 shows how ε varies with N for $\Omega_0 = 2\pi\times(200\text{ MHz})$ (red) and $\Omega_0 = 2\pi\times(100\text{ MHz})$ (blue) when only the effect of the imperfection of the π-pulses is considered. We see that $\varepsilon_{\text{max}} = 39$ for $N_{\text{opt}} = 69$ with $\Omega_0 = 2\pi\times(200\text{ MHz})$. With this Rabi frequency, when $N = 69$, the optimal Δ_0 is $2\pi\times(1.7\text{ GHz})$, according to Equation (25). It is also shown in Figure 11 that Ω_0 can significantly affect the maximum improvement LMT can achieve.

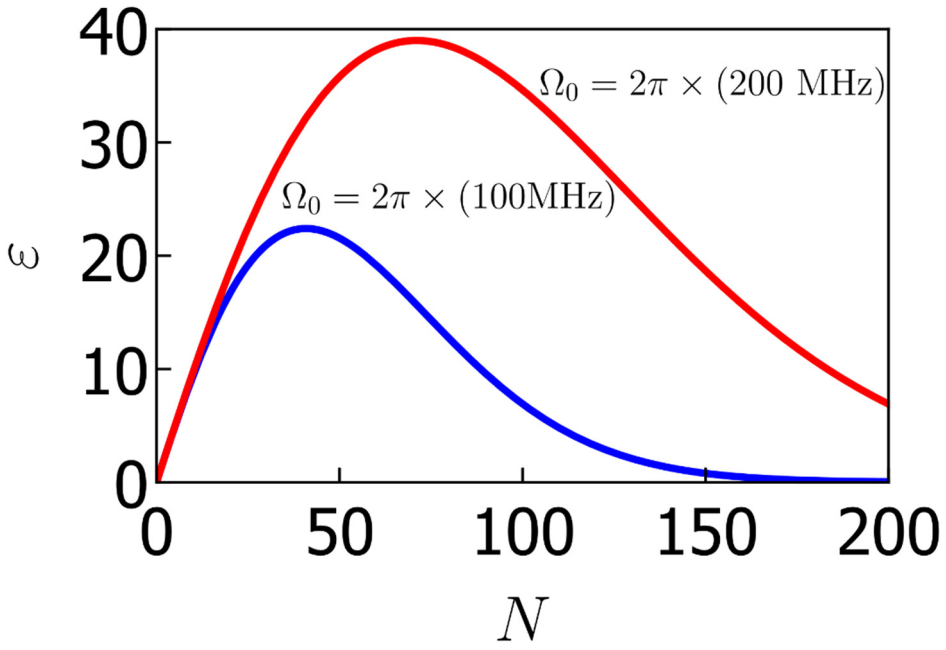

Figure 11. Improvement factor ε as a function of $N = k_t/k_{\text{eff}}$, with the effective Rabi frequency $\Omega_0 = 2\pi\times(200\text{ MHz})$ (red) and $\Omega_0 = 2\pi\times(100\text{ MHz})$ (blue) when only considering the effect of the imperfection of the π-pulses. For both curves, the improvement factor ε goes up first as N increases, then it reaches a maximum value, and finally goes down. The maximum improvement is also enhanced as Ω_0 increases. ε reaches a maximum value of 39 for N = 69 with $\Omega_0 = 2\pi\times(200\text{ MHz})$.

In the analysis above, we only considered the effect of imperfect π-pulses on the signal. Next, we incorporate the effect of the finite initial size discussed in Section 2 into the calculation of the signal. Adding the contribution of the finite initial size to the reduction in the height of the signal peak shown in Equation (4), Equation (23) is modified to be:

$$\ln h_{Nk_{\text{eff}}} \approx -\frac{1}{6}N^3\left(\frac{\hbar k_{\text{eff}}^2}{m\Omega_{\text{eff}}}\right)^2 - \frac{2\pi N\Gamma_{\text{eff}}}{\Omega_{\text{eff}}} - \frac{1}{2}(Nk_{\text{eff}}\Omega T\sigma_0)^2\left[1-\left(\frac{\sigma_0}{\sigma_f}\right)^2\right] - 2\ln 2 \tag{29}$$

and Equation (24) is modified to be:

$$\begin{aligned}\ln\varepsilon &= \ln N + \tfrac{1}{2}\ln\frac{h_{Nk_{\text{eff}}}}{h_{k_{\text{eff}}}}\\ &= \ln N - \tfrac{1}{3}N^3\left(\frac{\hbar k_{\text{eff}}^2\Delta_0}{m\Omega_0^2}\right)^2 - \frac{\pi N\Gamma}{2\Delta_0} - \tfrac{1}{4}(N^2-1)(k_{\text{eff}}\Omega T\sigma_0)^2\left[1-\left(\frac{\sigma_0}{\sigma_f}\right)^2\right]\\ &\approx \ln N - \tfrac{1}{3}N^3\left(\frac{\hbar k_{\text{eff}}^2\Delta_0}{m\Omega_0^2}\right)^2 - \frac{\pi N\Gamma}{2\Delta_0} - \tfrac{1}{4}(Nk_{\text{eff}}\Omega T\sigma_0)^2\left[1-\left(\frac{\sigma_0}{\sigma_f}\right)^2\right]\end{aligned} \tag{30}$$

Here, $\sigma_0\left(\sigma_f\right)$ is the initial (final) size of the atomic cloud, as defined earlier in Section 2. The optimal detuning will not be affected by the initial size of the atomic cloud because the term contributed by the finite initial size does not depend on the detuning Δ_0. Therefore, with the optimal detuning, we have:

$$\ln \varepsilon = \ln N - N^{5/3}\left(\frac{3\pi\Gamma\hbar k_{\mathrm{eff}}^2}{4m\Omega_0^2}\right)^{2/3} - \frac{1}{4}(Nk_{\mathrm{eff}}\Omega T\sigma_0)^2\left[1-\left(\frac{\sigma_0}{\sigma_{\mathrm{f}}}\right)^2\right] \tag{31}$$

Figure 12 shows the relationship between ε and N given by Equation (31), with $\sigma_{\mathrm{f}} = 1$ cm, $T_{\mathrm{K}} = 6$ μK, $\Omega_0 = 2\pi \times (200\,\mathrm{MHz})$. The black dotted curve shows the case where $\sigma_0 = 0$, which is identical to the red curve in Figure 12. The red curves are the plots for $\sigma_0 = 0.1$ mm, while the blue curves are for $\sigma_0 = 0.5$ mm. The solid (dashed) curves correspond to an angular velocity of 1 (2) μHz. We can see that if $\sigma_0 = 0.1$ mm, the correction to the signal due to the finite initial size is very small. In this case the conclusion derived above that $\varepsilon_{\mathrm{max}} = 39$ for $N_{\mathrm{opt}} = 69$ is still valid. We can also see that the correction to the signal due to the finite initial size decreases as the angular velocity we want to measure decreases. Therefore, LMT is more advantageous for measuring smaller rotations.

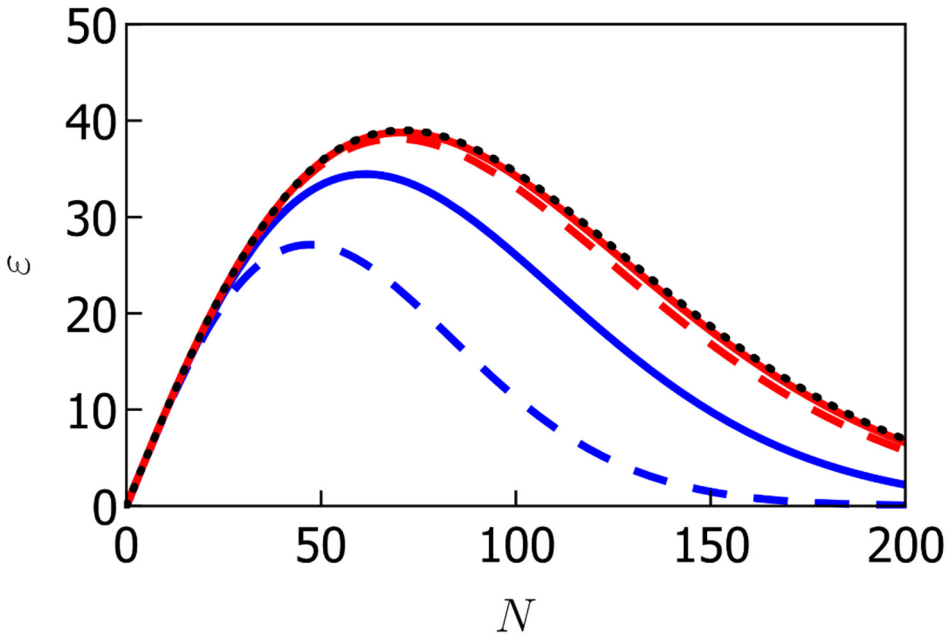

Figure 12. Relation between ε and N given by Equation (31), with $\sigma_{\mathrm{f}} = 1$ cm, $T_{\mathrm{K}} = 6$ μK, $\Omega_0 = 2\pi \times (200\,\mathrm{MHz})$. The black dotted curve shows the case where $\sigma_0 = 0$, which is identical to the red curve in Figure 11 because in this case there is no effect of the finite initial size of the atomic cloud. The red curves are the plots for $\sigma_0 = 0.1$ mm, while the blue curves are for $\sigma_0 = 0.5$ mm. The solid (dashed) curves correspond to an angular velocity of 1(2) μHz. We can see that the larger the initial size is, the less LMT can improve the PSI.

To recap, both Figures 11 and 12 are plots of the improvement factor ε versus $N \equiv k_{\mathrm{t}}/k_{\mathrm{eff}}$. Figure 11 shows the cases where we only considered the effect of Doppler shift detuning and spontaneous decay. Figure 12 shows the cases where we additionally took into account the effect of the finite initial size of the atomic cloud. In Figure 11, the blue curve shows the case where the one-photon Rabi frequency was 100 MHz and the red curve was 200 MHz. We can see that a higher one-photon Rabi frequency will enable us to improve the PSI more with LMT. We used a one-photon Rabi frequency of 200 MHz for all curves in Figure 12. In this figure, the red curves (both solid and dashed) are plots for the initial size of the atomic cloud $\sigma_0 = 0.1$ mm, and the blue curves for $\sigma_0 = 0.5$ mm. The solid curves (both red and blue) are for the angular velocity of 1 μHz, and the dashed curves are for 2 μHz. We can

see that both a smaller initial size and a smaller angular velocity will enable us to improve the PSI more with LMT. With $\Omega_0 = 2\pi \times 200$ MHz, $\sigma_0 = 0.1$ mm, and an angular velocity of 1 μHz, the effect of the finite initial size of the atomic cloud is not obvious and thus the result becomes very similar to the red curve in Figure 11 (reproduced as the black dotted curve in Figure 12).

It can be seen from the discussion above that the value of Ω_0 is very important for the performance of the LMT-PSI. Therefore, we discuss here the relationship between the experimental parameters and Ω_0. For ^{87}Rb, we assumed the ground state $|g\rangle$ to be $\{^2S_{1/2}, F = 1, m_F = 0\}$, and the excited state $|e\rangle$ to be $\{^2S_{1/2}, F = 2, m_F = 0\}$. In most implementations of Raman-pulse-based atom interferometers, the beams are circularly (σ) polarized [36]. If the beams are σ^+ polarized, the intermediate state $|i\rangle$ consists of two states: $|F = 1, m_F = 1\rangle$ and $|F = 2, m_F = 1\rangle$ of the $^2P_{3/2}$ manifold. The corresponding transition matrix elements [37] are shown in Figure 13. For the cycling transition from $|F = 2, m_F = 2\rangle$ to $|F = 3, m_F = 3\rangle$, an intensity of 3.34 mW/cm^2 yields $\Omega_0 = \Gamma$. For a given intensity on each leg of the Raman transition, we can use this information to determine the effective Rabi frequency for each of the two Raman transitions, treated separately, and the net effective Rabi frequency would be the sum of these two effective Rabi frequencies. If we assume that each leg has the same laser intensity and consider the fact that the energy separation between the two upper levels (~157 MHz) is negligible compared to the detuning, then it is easy to see that the effective Rabi frequency for the lower Raman transition is weaker than that for the upper Raman transition by a factor of $\left(\sqrt{1/8} \times \sqrt{1/8}\right) / \left(\sqrt{5/24} \times \sqrt{1/120}\right) = 3$. If we consider the upper Raman transition only, the intensity needed for the condition of $\Omega_0 = 2\pi \times (100 \text{ MHz}) \approx 16.7\Gamma$ is ~3.7 W/cm^2. When both Raman transitions are taken into account, an intensity lower by a factor of 3/4 (i.e., ~2.8 W/cm^2) would produce the effective Rabi frequency corresponding to $\Omega_0 = 16.7\Gamma$ in our model presented above [38]. Such an intensity can be achieved, for example, by using a tapered amplifier on each leg of the Raman transition.

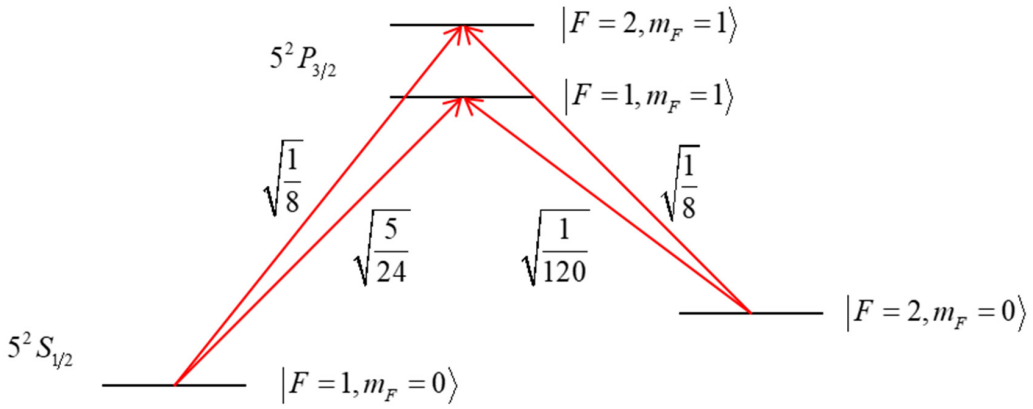

Figure 13. Matrix elements relevant to the Raman transition between $|g\rangle$ and $|e\rangle$.

There is another technique that can potentially decrease the effect of the detuning. At the beginning, when the momentum difference between the two arms is small, both arms are addressed with the same Raman beams. When the momentum difference between the two arms become large enough, we can address them with different Raman beams so that both arms are resonant to its own Raman beams and far detuned from the Raman beams for the other arm. This technique works well for very cold atoms. However, for an atom at a temperature of 6 μK, the thermal momentum is about $2\hbar k_{\text{eff}}$. It is not obvious whether this thermal momentum is sufficiently small in comparison to the total momentum transfer for this technique to improve the performance of the PSI–LMT significantly. This issue will be investigated in the future.

5. Conclusions

In a point source interferometer (PSI), atoms are split and recombined by applying a temporal sequence of Raman pulses during the expansion of a cloud of cold atoms behaving approximately as a point source. The PSI can work as a sensitive multi-axes gyroscope that automatically filters out the signal from accelerations, thus making it an attractive system for practical rotation sensing. The phase shift arising from rotations is proportional to the momentum transferred to each atom from the Raman pulses. Here, we investigated the degree of enhancement in sensitivity that could in principle be achieved by augmenting the PSI with large momentum transfer (LMT) employing a sequence of many Raman pulses with alternating directions. We considered a semi-classical model as well as an augmented quantum model under which the center-of-mass motion of atoms is treated quantum mechanically and showed that the results from these models are in close agreement with one another in the thermal limit, which applies to the situations we consider. After establishing this fact, we adopted the use of the semi-classical model for further analysis, since this allowed the derivation of analytical results regarding how the enhancement in sensitivity depends on the degree of large momentum transfer and the intensities of the Raman pulses, taking into account the effects of Doppler detuning and spontaneous emission. We have shown how increasing Doppler shifts leads to imperfections, thereby limiting the visibility of the signal fringes. We have also shown that this effect can be suppressed by increasing the effective Rabi frequencies of the Raman pulses. For a given value of the effective Rabi frequency, we showed that there is an optimum value for the number of pulses employed, beyond which the net enhancement in sensitivity begins to decrease. With LMT, the total duration of the pulses can be much longer than the conventional case, making the effect of spontaneous emission highly relevant. For a given one-photon Rabi frequency, a larger detuning decreases the effective Rabi frequency, but reduces spontaneous emission. Therefore, there exists an optimal detuning dependent on the number of pulses applied. For a given value of the one-photon Rabi frequency, employing the optimal detuning, we showed that there is an optimum value for the number of pulses used, beyond which the net enhancement in sensitivity begins to decrease. For a one-photon Rabi frequency of 200 MHz, for example, the peak value of the factor of enhancement in sensitivity is ~40, for a momentum transfer that is ~70 times as large as that for a conventional PSI. In addition to what we have studied here, other effects such as Rabi frequency inhomogeneities, AC Stark shifts, or laser wavefront imperfections may limit the sensitivity gained from implementing LMT. The impact of these effects on PSI will be modeled in future work. It is anticipated that composite pulses [17] or pulses employing adiabatic rapid passage [16], or optimal quantum control [39], which makes the transfer efficiency less sensitive to Doppler and AC-Stark-shift induced detunings and Rabi frequency inhomogeneities, would further increase the peak enhancement in sensitivity. Moreover, the implementation of PSI in combination with spatially resolved phase detection offers the potential to characterize and mitigate laser-wavefront-induced phase errors [1,40]. These and other mitigation strategies will be explored in future work.

Author Contributions: Conceptualization, S.M.S. and J.L.; methodology, S.M.S. and J.L.; software, J.L.; validation, all co-authors; formal analysis, J.L.; investigation, all co-authors; resources, S.M.S. and T.K.; data curation, not applicable; writing—original draft preparation, J.L., S.M.S. and T.K.; writing—review and editing, all co-authors; visualization, J.L.; supervision, S.M.S.; project administration, S.M.S.; funding acquisition, S.M.S. and T.K. All authors have read and agreed to the published version of the manuscript.

Funding: This work has been supported by NASA grant numbers 80NSSC19C0440 and 80NSSC20C0161, and ONR grant number N00014-19-1-2181.

Institutional Review Board Statement: Not necessary since this study did not involve any humans or animals.

Informed Consent Statement: Not necessary since this study did not involve any humans.

Data Availability Statement: Not necessary since this study did not use any data.

Conflicts of Interest: The authors declare no conflict of interest.

References and Note

1. Dickerson, S.M.; Hogan, J.M.; Sugarbaker, A.; Johnson, D.M.; Kasevich, M.A. Multiaxis inertial sensing with long-time point source atom interferometry. *Phys. Rev. Lett.* **2013**, *111*, 083001. [CrossRef]
2. Hoth, G.W.; Pelle, B.; Riedl, S.; Kitching, J.; Donley, E.A. Point source atom interferometry with a cloud of finite size. *Appl. Phys. Lett.* **2016**, *109*, 071113. [CrossRef]
3. Sugarbaker, A.; Dickerson, S.M.; Hogan, J.M.; Johnson, D.M.; Kasevich, M.A. Enhanced Atom Interferometer Readout through the Application of Phase Shear. *Phys. Rev. Lett.* **2013**, *111*, 113002. [CrossRef] [PubMed]
4. Kovachy, T.; Asenbaum, P.; Overstreet, C.; Donnelly, C.A.; Dickerson, S.M.; Sugarbaker, A.; Hogan, J.M.; Kasevich, M.A. Quantum superposition at the half-metre scale. *Nature* **2015**, *528*, 530–533. [CrossRef] [PubMed]
5. Asenbaum, P.; Overstreet, C.; Kovachy, T.; Brown, D.D.; Hogan, J.M.; Kasevich, M.A. Phase Shift in an Atom Interferometer due to Spacetime Curvature across its Wave Function. *Phys. Rev. Lett.* **2017**, *118*, 183602. [CrossRef]
6. Thomas, J.E.; Hemmer, P.R.; Ezekiel, S.; Leiby, C.C., Jr.; Picard, R.H.; Willis, C.R. Observation of Ramsey Fringes Using a Stimulated Resonance Raman Transition in a Sodium Atomic Beam. *Phys. Rev. Lett.* **1982**, *48*, 867–870. [CrossRef]
7. Bordé, C.J. Atomic interferometry with internal state labelling. *Phys. Lett. A* **1989**, *140*, 10. [CrossRef]
8. Kasevich, M.; Chu, S. Atomic interferometry using stimulated Raman transitions. *Phys. Rev. Lett.* **1991**, *67*, 181. [CrossRef]
9. Canuel, B.; Leduc, F.; Holleville, D.; Gauguet, A.; Fils, J.; Virdis, A.; Clairon, A.; Dimarcq, N.; Bordé, C.J.; Landragin, A.; et al. Six-Axis Inertial Sensor Using Cold-Atom Interferometry. *Phys. Rev. Lett.* **2006**, *97*, 010402. [CrossRef]
10. Barrett, B.; Geiger, R.; Dutta, I.; Meunier, M.; Canuel, B.; Gauguet, A.; Bouyer, P.; Landragin, A. The Sagnac effect: 20 years of development in matter-wave interferometry. *Comptes Rendus Phys.* **2014**, *15*, 875–883. [CrossRef]
11. Barrett, B.; Cheiney, P.; Battelier, B.; Napolitano, F.; Bouyer, P. Multidimensional Atom Optics and Interferometry. *Phys. Rev. Lett.* **2019**, *122*, 043604. [CrossRef]
12. Gustavson, T.L.; Landragin, A.; Kasevich, M.A. Rotation sensing with a dual atom-interferometer Sagnac gyroscope. *Class. Quantum Grav.* **2000**, *17*, 2385. [CrossRef]
13. Müller, T.; Gilowski, M.; Zaiser, M.; Berg, P.; Schubert, C.; Wendrich, T.; Ertmer, W.; Rasel, E.M. compact dual atom interferometer gyroscope based on laser-cooled rubidium. *Eur. Phys. J. D* **2009**, *53*, 273–281. [CrossRef]
14. Hoth, G.W.; Pelle, B.; Kitching, J.; Donley, E.A. Trade-offs in size and performance for a point source interferometer gyroscope. In Proceedings of the 2017 IEEE International Symposium on Inertial Sensors and Systems (INERTIAL), Kauai, HI, USA, 28–30 March 2017; pp. 4–7.
15. Sarkar, R.; Fang, R.; Shahriar, S.M. High-Compton-frequency, parity-independent, mesoscopic Schrödinger-cat-state atom interferometer with Heisenberg-limited sensitivity. *Phys. Rev. A* **2018**, *98*, 013636. [CrossRef]
16. Shahriar, M.S.; Jheeta, M.; Tan, Y.; Pradhan, P.; Gangat, A. Continuously Guided Atomic Interferometry Using a Single-Zone Optical Excitation: Theoretical Analysis. *Opt. Commun.* **2004**, *243*, 183–201. [CrossRef]
17. Tino, G.M.; Kasevich, M.A. *Atom Interferometry*; IOS Press: Amsterdam, The Netherlands, 2014.
18. Smith, E.T.; Dhirani, A.A.; Kokorowski, D.A.; Rubenstein, R.A.; Roberts, T.D.; Yao, H.; Pritchard, D.E. Velocity rephased longitudinal momentum coherences with differentially detuned separated oscillatory fields. *Phys. Rev. Lett.* **1998**, *81*, 1996. [CrossRef]
19. Golub, R.; Lamoreaux, S.K. Elucidation of the neutron coherence length and a matter-wave sideband interferometer. *Phys. Lett. A* **1992**, *162*, 122–128. [CrossRef]
20. You, L.; Holland, M. Ballistic expansion of trapped thermal atoms. *Phys. Rev. A* **1996**, *53*, R1. [CrossRef]
21. Fouda, M.F.; Fang, R.; Ketterson, J.B.; Shahriar, M.S. Generation of Arbitrary Lithographic Patterns Using BEC Interferometry. *Phys. Rev. A* **2016**, *94*, 063644. [CrossRef]
22. McGuirk, J.M.; Snadden, M.J.; Kasevich, M.A. Large Area Light-Pulse Atom Interferometry. *Phys. Rev. Lett.* **2000**, *85*, 4498. [CrossRef] [PubMed]
23. Kotru, K.; Butts, D.L.; Kinast, J.M.; Stoner, R.E. Large-Area Atom Interferometry with Frequency-Swept Raman Adiabatic Passage. *Phys. Rev. Lett.* **2015**, *115*, 103001. [CrossRef] [PubMed]
24. Butts, D.L.; Kotru, K.; Kinast, J.M.; Radojevic, A.M.; Timmons, B.P.; Stoner, R.E. Efficient broadband Raman pulses for large-area atom interferometry. *JOSA B* **2013**, *30*, 922–927. [CrossRef]
25. Chiow, S.W.; Kovachy, T.; Chien, H.C.; Kasevich, M.A. 102$\hbar$k Large Area Atom Interferometers. *Phys. Rev. Lett.* **2011**, *107*, 130403. [CrossRef]
26. Overstreet, C.; Asenbaum, P.; Kovachy, T.; Notermans, R.; Hogan, J.M.; Kasevich, M.A. Effective Inertial Frame in an Atom Interferometric Test of the Equivalence Principle. *Phys. Rev. Lett.* **2018**, *120*, 183604. [CrossRef]
27. Cladé, P.; Guellati-Khélifa, S.; Nez, F.; Biraben, F. Large Momentum Beam Splitter Using Bloch Oscillations. *Phys. Rev. Lett.* **2009**, *102*, 240402. [CrossRef]
28. Müller, H.; Chiow, S.W.; Herrmann, S.; Chu, S. Atom Interferometers with Scalable Enclosed Area. *Phys. Rev. Lett.* **2009**, *102*, 240403. [CrossRef] [PubMed]

29. McDonald, G.D.; Kuhn, C.C.; Bennetts, S.; Debs, J.E.; Hardman, K.S.; Johnsson, M.; Close, J.D.; Robins, N.P. 80$\hbar$k momentum separation with Bloch oscillations in an optically guided atom interferometer. *Phys. Rev. Lett.* **2013**, *88*, 053620.
30. Gebbe, M.; Siemß, J.N.; Gersemann, M.; Müntinga, H.; Herrmann, S.; Lämmerzahl, C.; Ahlers, H.; Gaaloul, N.; Schubert, C.; Hammerer, K.; et al. Twin-lattice atom interferometry. *Nat. Commun.* **2021**, *12*, 2544. [CrossRef]
31. Müller, H.; Chiow, S.W.; Long, Q.; Herrmann, S.; Chu, S. Atom Interferometry with up to 24-Photon-Momentum-Transfer Beam Splitters. *Phys. Rev. Lett.* **2008**, *100*, 180405. [CrossRef] [PubMed]
32. Hemmer, P.; Shahriar, M.S.; Natoli, V.; Ezekiel, S. AC-Stark Shifts in a Two Zone Raman interaction. *J. Opt. Soc. Am. B* **1989**, *6*, 1519. [CrossRef]
33. Rudolph, J.; Wilkason, T.; Nantel, M.; Swan, H.; Holland, C.M.; Jiang, Y.; Garber, B.E.; Carman, S.P.; Hogan, J.M. Large Momentum Transfer Clock Atom Interferometry on the 689 nm Intercombination Line of Strontium. *Phys. Rev. Lett.* **2020**, *124*, 083604. [CrossRef]
34. Barrett, B.; Carew, A.; Beica, H.C.; Vorozcovs, A.; Pouliot, A.; Kumarakrishnan, A. Prospects for Precise Measurements with Echo Atom Interferometry. *Atoms* **2016**, *4*, 19. [CrossRef]
35. Shahriar, M.S.; Hemmer, P.R.; Katz, D.P.; Lee, A.; Prentiss, M.G. Dark-State-Based Three-element Vector Model for the Resonant Raman Interaction. *Phys. Rev. A* **1997**, *55*, 2272. [CrossRef]
36. Chen, Y.J.; Hansen, A.; Hoth, G.W.; Ivanov, E.; Pelle, B.; Kitching, J.; Donley, E.A. Single-Source Multiaxis Cold-Atom Interferometer in a Centimeter-Scale Cell. *Phys. Rev. Appl.* **2019**, *12*, 014019. [CrossRef]
37. Steck, D. Rubidium 87 D Line Data. Available online: https://steck.us/alkalidata/rubidium87numbers.1.6.pdf (accessed on 2 August 2021).
38. Such a configuration would produce differences in the light shifts experienced by the two ground states. This can be compensated for by adjusting the two-photon detuning of the Raman beams. Alternatively, the relative intensities on the two legs can be adjusted to balance the light shifts.
39. Saywell, J.C.; Kuprov, I.; Goodwin, D.; Carey, M.; Freegarde, T. Optimal control of mirror pulses for cold-atom interferometry. *Phys. Rev. A* **2018**, *98*, 023625. [CrossRef]
40. Abe, M.; Adamson, P.; Borcean, M.; Bortoletto, D.; Bridges, K.; Carman, S.P.; Chattopadhyay, S.; Coleman, J.; Curfman, N.M.; DeRose, K.; et al. Matter-wave Atomic Gradiometer Interferometric Sensor (MAGIS-100). *Quantum Sci. Technol.* **2021**, in press. [CrossRef]